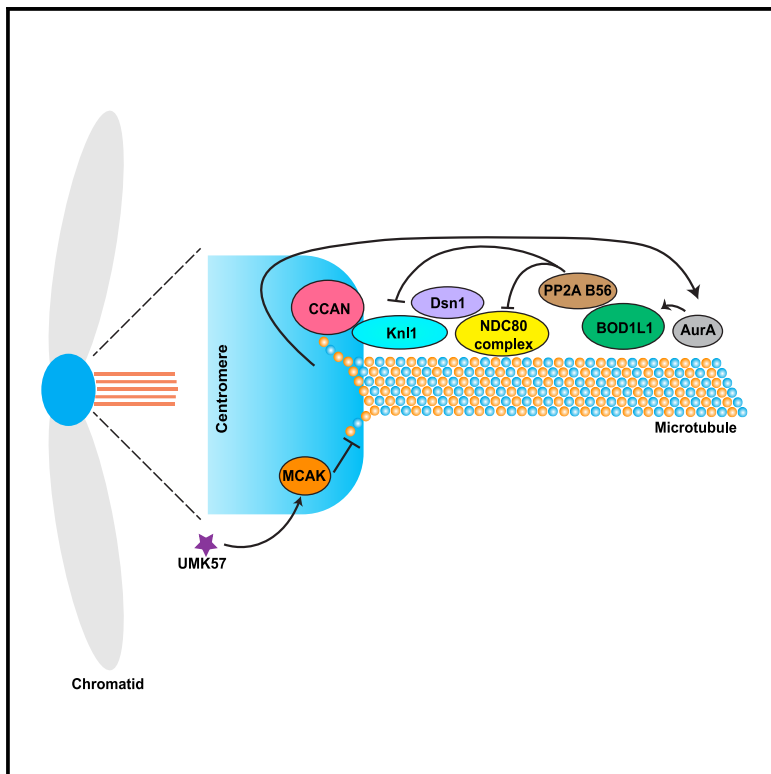


An Aurora kinase A-BOD1L1-PP2A B56 axis promotes chromosome segregation fidelity

Graphical abstract



Authors

Thomas J. Kucharski, Irma M. Vlasac,
Tatiana Lyalina, Martin R. Higgs,
Brock C. Christensen,
Susanne Bechstedt, Duane A. Compton

Correspondence

duane.a.compton@dartmouth.edu

In brief

Kucharski et al. identify a new signaling pathway in mitosis whereby Aurora kinase A phosphorylates BOD1L1 to increase protein phosphatase activity toward kinetochore substrates to facilitate high mitotic fidelity. This pathway provides the mechanism for adaptive resistance in cancer cells to an agonist of microtubule depolymerase.

Highlights

- BOD1L1 was identified in a screen to discover the mechanism of resistance to an MCAK agonist
- Aurora kinase A phosphorylates BOD1L1 to regulate PP2A activity at the kinetochore
- BOD1L1 localizes to the mitotic spindle and kinetochores and regulates faithful mitosis
- BOD1L1 loss increases sensitivity of cancer cells to relevant doses of Taxol



Article

An Aurora kinase A-BOD1L1-PP2A B56 axis promotes chromosome segregation fidelity

Thomas J. Kucharski,^{1,2} Irma M. Vlasac,³ Tatiana Lyalina,² Martin R. Higgs,⁴ Brock C. Christensen,^{3,5,6,7} Susanne Bechstedt,^{2,8} and Duane A. Compton^{1,9,*}

¹Department of Biochemistry and Cell Biology, Geisel School of Medicine at Dartmouth, Hanover, NH 03755, USA

²Department of Anatomy and Cell Biology, McGill University, Montréal, QC H3A 0C7 Canada

³Department of Epidemiology, Geisel School of Medicine at Dartmouth, Lebanon, NH 03756, USA

⁴Institute of Cancer and Genomic Sciences, University of Birmingham, Birmingham B15 2TT, UK

⁵Department of Molecular and Systems Biology, Geisel School of Medicine at Dartmouth, Lebanon, NH 03756, USA

⁶Department of Community and Family Medicine, Geisel School of Medicine at Dartmouth, Lebanon, NH 03756, USA

⁷Dartmouth Cancer Center, Geisel School of Medicine at Dartmouth, Lebanon, NH 03756, USA

⁸Centre de Recherche en Biologie Structurale, McGill University, Montréal, QC H3G 0B1 Canada

⁹Lead contact

*Correspondence: duane.a.compton@dartmouth.edu

<https://doi.org/10.1016/j.celrep.2025.115317>

SUMMARY

Cancer cells are often aneuploid and frequently display elevated rates of chromosome mis-segregation, called chromosomal instability (CIN). CIN is caused by hyperstable kinetochore-microtubule (K-MT) attachments that reduce the correction efficiency of erroneous K-MT attachments. UMK57, a chemical agonist of the protein MCAK (mitotic centromere-associated kinesin), improves chromosome segregation fidelity in CIN cancer cells by destabilizing K-MT attachments, but cells rapidly develop resistance. To determine the mechanism, we performed unbiased screens, which revealed increased phosphorylation in cells adapted to UMK57 at Aurora kinase A phosphoacceptor sites on BOD1L1 (protein biorientation defective 1-like-1). BOD1L1 depletion or Aurora kinase A inhibition eliminated resistance to UMK57. BOD1L1 localizes to spindles/kinetochores during mitosis, interacts with the PP2A phosphatase, and regulates phosphorylation levels of kinetochore proteins, chromosome alignment, mitotic progression, and fidelity. Moreover, the *BOD1L1* gene is mutated in a subset of human cancers, and *BOD1L1* depletion reduces cell growth in combination with clinically relevant doses of Taxol or Aurora kinase A inhibitor.

INTRODUCTION

Faithful chromosome segregation during cell division relies on bioriented attachment of kinetochores to spindle microtubules. Errors in kinetochore-microtubule (K-MT) attachment arise frequently during early phases of mitosis, and the persistence of these errors is a common cause of chromosomal instability (CIN) and aneuploidy in solid tumors.^{1–5} We have demonstrated previously that destabilizing K-MT attachments promotes faithful chromosome segregation in CIN cancer cells by increasing the correction rate of K-MT attachment errors. Specifically, overexpression of either MCAK (alias KIF2C) or KIF2B microtubule depolymerases suppressed chromosome mis-segregation in CIN cancer cell lines.^{5–8} These data demonstrate the potential of suppressing CIN as a strategy for cancer treatment.

To pursue this strategy, we recently characterized a cell-permeable small-molecule agonist of MCAK activity called UMK57. MCAK plays a key role at centromeres/kinetochores by increasing K-MT turnover to facilitate error correction prior to anaphase.^{9,10} At moderate dosage (100 nM), UMK57 increases the rate of K-MT detachment and decreases the rate of chromosome mis-segregation. Surprisingly, high rates of chromosome mis-segregation re-

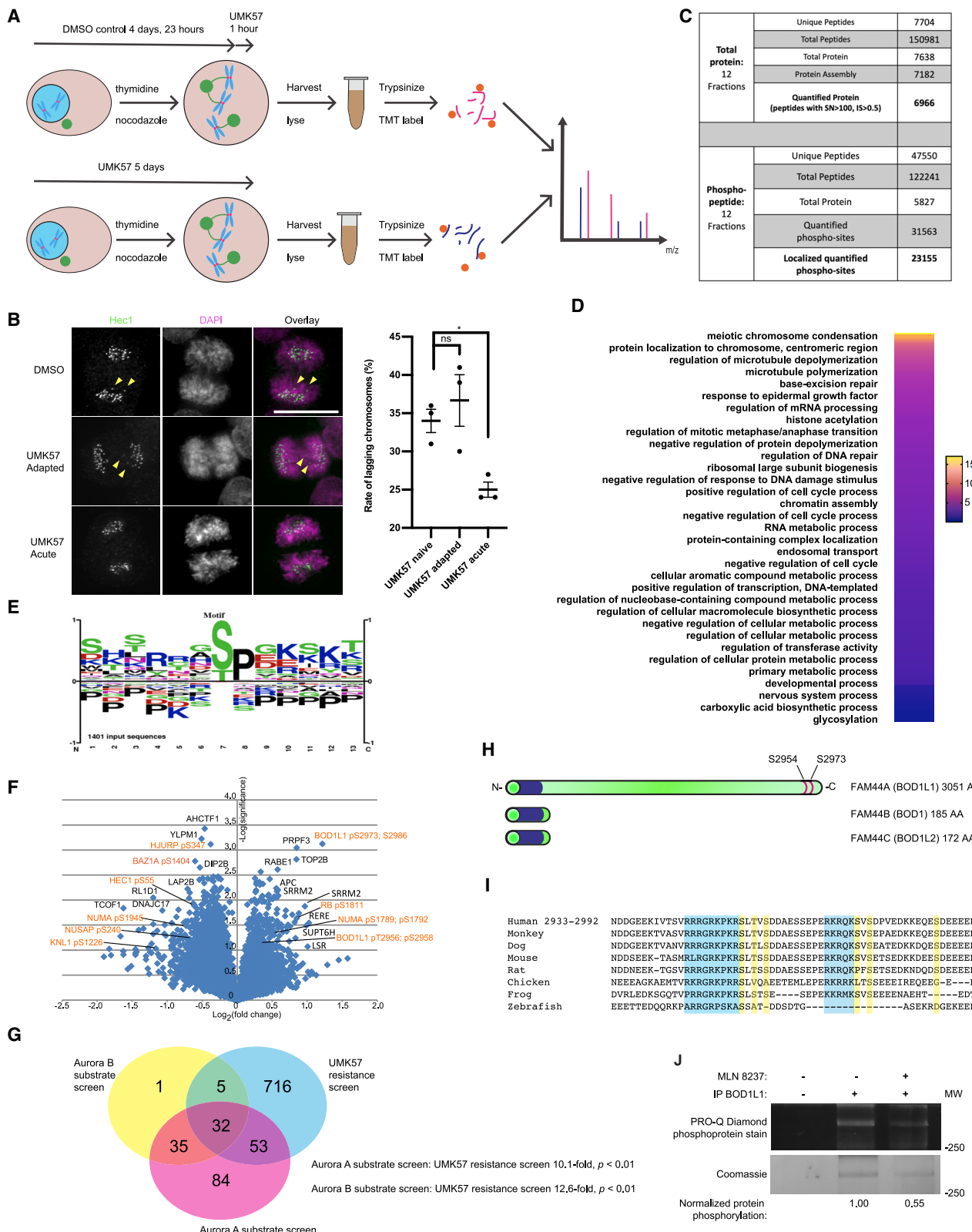
turned to CIN cancer cells after only ~72 h of UMK57 treatment. This resistance arose within the entire cell population, did not depend on the activity of drug efflux pumps, and did not occur due to drug lability, changes in the level or localization of MCAK, or changes to overall spindle morphology, and data demonstrated that MCAK continued to be activated by UMK57 in treated cells. Thus, this represents adaptive resistance (as opposed to acquired resistance, which relies on the emergence of rare genetic variants) to UMK57 whereby changes to cell signaling pathways bypass increased MCAK activity. Here, we use unbiased proteomics screens to identify the mechanism of resistance through an Aurora kinase A (AurKA)-BOD1L1-PP2A axis.

RESULTS

Proteomics analysis of UMK57 resistance in mitotic cells

To investigate the mechanisms promoting resistance to UMK57, we developed conditions for proteomics screens in mitotic cells (Figure 1A). We utilized SW620 cells because they have CIN and they undergo adaptive resistance to UMK57.¹¹ Specifically, SW620 cells naive to UMK57 display lagging chromosomes in





(legend on next page)

34% of anaphases. The rate of lagging chromosomes in anaphase decreases to 25% upon treatment with 100 nM UMK57 for 1 h and rebounds to 37% following 72 h of continuous treatment (Figure 1B). SW620 cells also display reduced phosphorylation of MCAK pS95 and AurKB pT232 following 72 h of treatment with UMK57, consistent with our previous findings indicating that changes in centromere/kinetochore phosphorylation levels correlated with adaptive resistance (Figures S1A–S1D).

For comparison of total protein levels between cells acutely treated with UMK57 and UMK57-adapted cells (Figure 1A), we obtained data for 6,966 proteins based on 7,704 unique and 15,0981 total peptides (Figure 1C). Among these, protein levels between the two cell populations varied from +1.725- to 0.41-fold change, with 6,813 proteins (97.7%) varying between the two cell populations within +1.2- and 0.8-fold-change. Protein levels skewed toward increased levels in one biological replicate, resulting in a skewed overall distribution (Figure S1E; Table S1). Among the proteins identified, the levels of Sgo2 were significantly increased (#38, +1.30-fold, $p = 0.0037$, 6 peptides) in adapted cells,^{13,14} although independent validation of the Sgo2 protein level change was inconclusive (Figure S1F). Thus, total protein levels in mitotic SW620 cells that have adapted to UMK57 change very little, and within a narrow range, relative to mitotic SW620 cells that are acutely treated with UMK57.

We next examined the phospho-proteomic changes in mitotic SW620 cells that have adapted to UMK57 versus cells that are acutely treated. We obtained data from 47,550 unique peptides from 122,241 total peptides. Of these, 31,563 sites were quantified, and 23,155 sites were both quantified and localized (Figure 1C; Table S2). Phospho-peptide levels between the two cell populations varied from 2.98- to 0.27-fold change, with 19,973 (86.2%) varying between the two cell populations within 1.2- to 0.8-fold change. Of the 1,169 peptides showing significant changes in peptide phosphorylation ($p < 0.1$), only 237 were increased, suggesting a broad decrease in phosphorylation in cells adapted to UMK57.

Gene Ontology analysis of the proteins that displayed significant changes in peptide phosphorylation ($p < 0.1$) revealed significant over-representation of proteins involved in mitotic processes, including chromosome condensation, centromere/chromosome localization, and microtubule polymerization and de-polymerization, consistent with an adaptive resistance to UMK57 altering mitotic processes (Figure 1D). Search Tool for the Retrieval of Interacting Genes/Proteins interaction network analysis of the top and bottom 100 proteins displaying significant changes in peptide phosphorylation revealed a cluster of proteins involved in mitosis. Of these, proteins with peptides displaying significantly increased levels of phosphorylation in adapted cells relative to acutely treated cells include Numa, 53BP1, Ska3, INCENP (inner centromere protein), and BOD1L1 (alias FAM44A). Proteins with peptides displaying significantly decreased levels of phosphorylation in adapted cells relative to acutely treated cells included Kn1, Numa, Hec1, nucleolar and spindle associated protein-1, INCENP, and TPX2 (targeting protein for Xklp2) (Figure 1F; Table S2).

Phosphoacceptor sites identified in the screen with significant changes in phosphorylation level ($p < 0.1$) showed over-representation of the canonical Cdk phosphorylation site motif (S/TPxxK) and possibly Aurora kinase motifs (R/KR/KxS/T) (Figure 1E). Comparisons to a previous screen that identified Aurora-dependent phosphoacceptor sites in mitosis¹² and that categorized peptides as being AurKA or AurKB targets revealed a 10.1- and 12.6-fold over-representation of AurKA substrates and AurKB substrates, respectively, among the population of phosphoacceptor sites identified in our dataset, although many phosphoacceptor sites could be phosphorylated by both kinases (Figure 1G).

Among all proteins that displayed changes in phosphorylation level in adapted cells relative to acutely treated cells, BOD1L1 demonstrated the most significant change. 32 different BOD1L1 phospho-peptides were detected in the phospho-proteomics screen, of which 3 showed statistically significant positive changes and two statistically significant negative changes.

Figure 1. Proteomics screening identifies BOD1L1

- (A) Experimental schematic of the proteomics screen. SW620 cells were treated for 3 days with UMK57 or the DMSO control and then synchronized by thymidine-nocodazole treatment. The DMSO control sample was treated with UMK57 for 1 h. Cells were collected and analyzed by mass spectrometry.
- (B) SW620 cells were prepared as in (A) but re-plated on glass coverslips instead of synchronization. After 24 h, cells were fixed and stained for Hec1 and DAPI, and the frequency of lagging chromosomes was measured. Statistical significance was calculated using Dunnett's multiple-comparison test. Representative images from 3 independent experiments are shown. The images were adjusted evenly for brightness and contrast. Scale bar, 10 μm . * $p < 0.05$.
- (C) SW620 cells were prepared as in (A) and analyzed by mass spectrometry. The number of peptides and proteins detected in the screens are shown.
- (D) Proteins from the phospho-proteomics screen that were significantly changed ($p < 0.1$) by Student's t test were analyzed for gene ontology. The data were then transferred to Prism software and plotted.
- (E) Proteins from the phospho-proteomics screen that were significantly changed ($p < 0.1$) by Student's t test were analyzed by PhosphositePlus for sequence motif enrichment and plotted.
- (F) Volcano plot analysis of the phospho-proteomics screen results. Proteins of potential interest are highlighted in orange. Statistical significance was calculated using two-tailed t tests.
- (G) Analysis of overlap between the phospho-proteomics study presented here and a previous study.¹² Proteins with changes in phosphorylation greater than 4-fold caused by AurKA or AurKB inhibitors were considered targets of AurKA or AurKB. The list of Aurora A and Aurora B targets was compared to the list of proteins from the phospho-proteomics screen that had significantly changed phosphorylation sites ($p < 0.1$) by Student's t test.
- (H) Schematic of the FAM44 protein family, showing the Bod1-similar domain and potential AurKA sites on BOD1L1. Scales are approximate.
- (I) Amino acid sequence alignment of BOD1L1 orthologs from residues 2,933–2,992 (relative to the human sequence). Residues highlighted in pink indicate Aurora kinase-defining motifs. Residues highlighted in yellow indicate potential phosphorylation sites.
- (J) SW620 cells were synchronized and treated with DMSO or MLN8237. BOD1L1 or control immunoprecipitations were performed, and the entire was separated by SDS-PAGE and stained with ProQ Diamond phosphoprotein stain, imaged, and subsequently stained with Coomassie blue and re-imaged. Two independent experiments were performed with similar results.

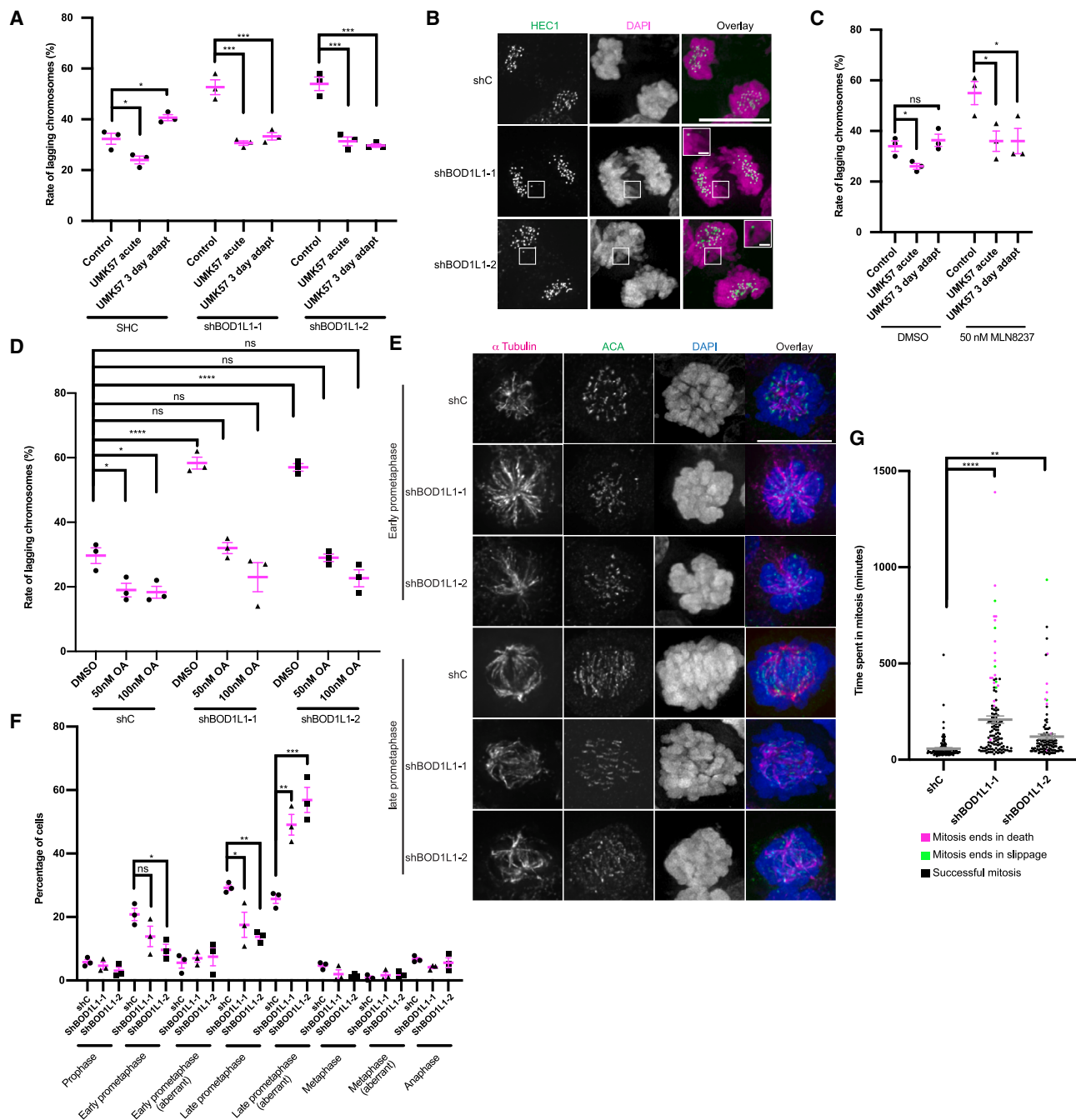


Figure 2. BOD1L1 and Aurora A are required for adaptation to UMK57 and mitotic fidelity

(A) SW620 cells were transfected with control shRNA or shRNA against BOD1L1. Cells were fixed and stained for Hec1 and DAPI. Cells were treated with DMSO or UMK57 for 1 h or 72 h. The percentage of lagging chromosomes in anaphase for cells expressing the indicated shRNA is shown. 100 cells per shRNA and condition were scored for each of 3 independent biological repeats. Error bars indicate the mean \pm SEM. * $p < 0.05$, ** $p < 0.001$. Statistical significance was calculated between the indicated conditions using Dunnett's multiple-comparisons test.

(B) SW620 cells were transfected with control shRNA or shRNA against BOD1L1. Cells were fixed and stained for Hec1 and DAPI. Cells were treated with DMSO or UMK57 for 1 h or 72 h. Representative images from 3 independent experiments are shown. The images were adjusted evenly for brightness and contrast. Scale bars, 10 μ m and 1 μ m (inset).

(C) SW620 were treated with DMSO or MLN8237 with or without UMK57. After 72 h, the cells were fixed and stained for Hec1 and DAPI. The percentage of lagging chromosomes in anaphase for cells expressing the indicated shRNA is shown. 100 cells per shRNA and condition were scored for each of 3 independent biological repeats. Error bars indicate the mean \pm SEM. * $p < 0.05$, ** $p < 0.001$. Statistical significance was calculated between the indicated conditions using Dunnett's multiple-comparisons test.

(legend continued on next page)

BOD1L1 (FAM44A) is closely related to Bod1 (FAM44B) and Bod1L2 (FAM44C) but contains a short proline-rich N-terminal extension and a long C-terminal extension (Figure 1H). Phosphoacceptors on BOD1L1 displaying significant increases in phosphorylation in adapted cells include T2956 and S2958 (1.3-fold, $p = 0.06$), S2973 and 2986 (2.3-fold, $p < 0.01$), and S2986 (1.2-fold, $p = 0.07$). Importantly, the total protein level of BOD1L1 did not change in adapted cells relative to acutely treated cells (1.06-fold, $p = 0.26$, 15 peptides) (Figure 1F; Table S1), indicating that BOD1L1 undergoes net changes in phosphorylation status as cell adapt to UMK57. The peptide containing S2954, T2956, and S2958 has been identified previously in a phospho-proteomics screen¹² and suggested to be selectively phosphorylated by AurKA based on the conserved cluster of lysine and arginine residues proximal to the phosphoacceptor site (Figure 1I) and sensitivity to an AurKA inhibitor (Figure S1H).¹² Moreover, BOD1L1 has been detected previously in an AurKA proximity ligation mapping experiment.¹⁵

To confirm that BOD1L1 is phosphorylated by AurKA, we treated nocodazole-synchronized mitotic cells with DMSO or an AurKA inhibitor, purified BOD1L1, and demonstrated a substantial decrease in BOD1L1 phosphorylation in AurKA inhibitor-treated cells (Figure 1J). We next incubated the purified C-terminal fragment of BOD1L1 containing the phosphorylation sites that we identified in our mass spectrometry dataset together with AurKA and demonstrated ATP- and AurKA-dependent phosphorylation (Figure S1I). Furthermore, AurKA failed to phosphorylate BOD1L1 when the phosphoacceptor sites we detected in our dataset were mutated to alanine (referred to as F6A) (Figure S1J). Thus, Aurora A phosphorylates BOD1L1 on the phosphoacceptor residues detected in our mass spectrometry dataset *in vitro* and in mitotic cells. These data demonstrate that BOD1L1 is selectively phosphorylated by AurKA as cells adapt to UMK57.

BOD1L1 and AurKA are required for adaptation to UMK57

To determine whether BOD1L1 is required for adaptive resistance to UMK57 in CIN cancer cells, we used two independent shRNA (short hairpin RNA) sequences to knock down BOD1L1 expression. We confirmed durable knockdown of BOD1L1 in cells expressing BOD1L1 shRNA compared to cells expressing control shRNA using BOD1L1-specific antibodies on immunoblot and through indirect immunofluorescence (Figures S2A and S2B).

Next, we tested whether BOD1L1 is required for cells to adapt to UMK57. We transfected cells with BOD1L1-specific shRNA-

or control shRNA-expressing plasmids, selected for puromycin resistance, added UMK57 for short or prolonged periods, and measured the frequency of lagging chromosomes during mitosis. As expected in cells transfected with control shRNA, acute treatment with UMK57 reduced the frequency of lagging chromosomes in anaphase, and high lagging chromosome rates returned upon prolonged treatment with UMK57. Cells transfected with shRNA against BOD1L1 displayed elevated rates of lagging chromosomes in anaphase compared to control cells. Despite the identified role of BOD1L1 in DNA repair, the increased rate of lagging chromosomes we observed in BOD1L1 knockdown cells was not likely to be due to elevated levels of DNA damage, as there was no increase in basal levels of DNA repair foci in knockdown cells compared to control cells prior to irradiation.¹⁶ BOD1L1-deficient cells responded to acute treatment with UMK57 and showed significantly fewer anaphase cells with lagging chromosomes. The effect of UMK57 on BOD1L1-deficient cells was durable because cells retained significantly reduced lagging chromosome rates compared to DMSO-treated cells throughout prolonged treatment (Figures 2A and 2B). Therefore, BOD1L1 is required for adaptation to prolonged UMK57 treatment.

We also tested whether AurKA activity is required for adaptation to UMK57 using a sublethal 50 nM dose of an AurKA inhibitor. SW620 cells continued to proliferate in the presence of the AurKA inhibitor (Figure S2C), and cells treated with the AurKA inhibitor alone displayed elevated levels of lagging chromosomes compared to cells treated with DMSO. Cells treated with the AurKA inhibitor responded to acute treatment with UMK57 and displayed significantly fewer lagging chromosomes relative to cells treated with the AurKA inhibitor alone. The fraction of anaphase cells with lagging chromosomes remained significantly reduced in cells with prolonged UMK57 treatment when AurKA was inhibited, demonstrating that AurKA is also required for adaptation to UMK57 treatment (Figure 2C).

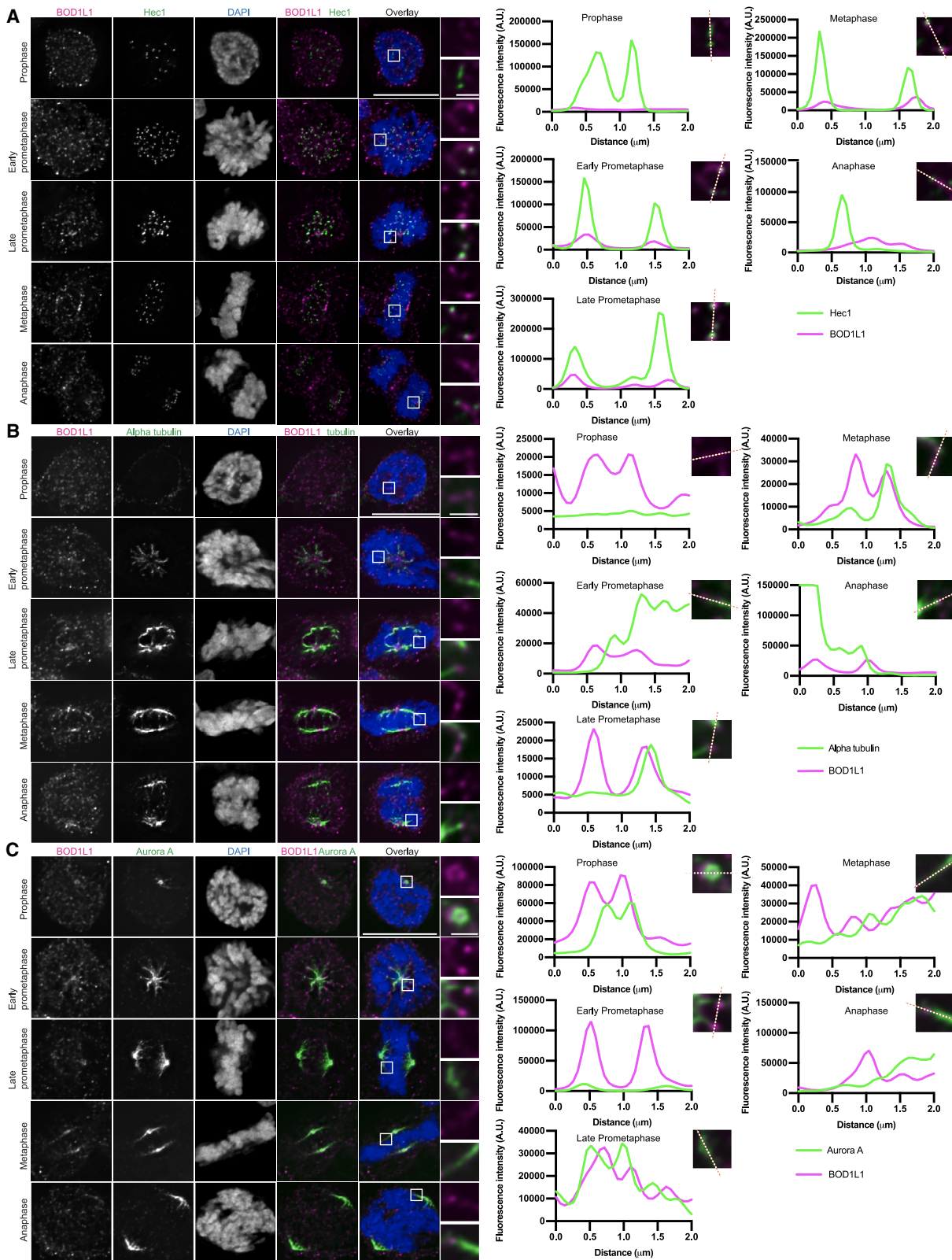
These and previous data¹¹ indicate that adaptation to UMK57 treatment likely occurs through changes in kinetochore protein phosphorylation. Therefore, we tested whether treatment of cells with a modest dose of okadaic acid (a PP2A/PP1 inhibitor)¹⁷ would alter the rate of lagging chromosomes in anaphase. Cells transfected with control shRNA displayed a reduced frequency of lagging chromosomes when treated with okadaic acid, suggesting that elevated protein phosphorylation can increase chromosome segregation fidelity (Figure 2D). As expected, BOD1L1-deficient cells displayed elevated numbers of lagging chromosomes. Remarkably, cells transfected with shRNA

(D) SW620 cells were transfected with control shRNA or shRNA against BOD1L1. Cells were treated with DMSO or okadaic acid for 90 min prior to fixation. The cells were then stained for Hec1 and DAPI. The percentage of lagging chromosomes in anaphase for cells expressing the indicated shRNA is shown. 100 cells per shRNA and condition were scored for each of 3 independent biological repeats. Error bars indicate the mean \pm SEM. * $p < 0.05$, ** $p < 0.001$. Statistical significance was calculated between the indicated conditions using Dunnett's multiple-comparisons test.

(E) Immunofluorescence images of SW620 cells transfected with control shRNA or shRNA against BOD1L1. The cells were then fixed and stained for α -tubulin and ACA (anti-centromere antibody). Representative images of 2 independent biological experiments are shown. The images were adjusted evenly for brightness and contrast. Scale bar, 10 μ m.

(F) Quantification of the cells shown in (A). Statistical significance was calculated between the indicated conditions using Dunnett's multiple-comparisons test. * $p < 0.05$, ** $p < 0.01$, *** $p < 0.001$.

(G) SW620 cells were co-transfected with control shRNA or shRNA against BOD1L1 together with mCherry-H2B. Following selection, time-lapse imaging was started at 5-min intervals. The fate of at least 40 cells per experiment for each of 3 independent biological repeats was recorded. Statistical significance was calculated between the indicated conditions using Dunnett's multiple-comparison test. ** $p < 0.01$, *** $p < 0.0001$.



(legend on next page)

against BOD1L1 and treated with okadaic acid had rates of lagging chromosomes in anaphase that were not different from control shRNA/DMSO-treated cells. Thus, okadaic acid treatment effectively replaces BOD1L1 function in mitosis.

BOD1L1 regulates mitotic progression and mitotic fidelity

To date, the only role identified for BOD1L1 is in DNA repair.^{16,18,19} BOD1L1 shares extensive sequence similarity with BOD1, which has been shown to be involved in regulation of mitotic activities, including kinetochore protein phosphorylation by recruiting the PP2A-B56 phosphatase and regulating MCAK localization, and to be important for chromosome alignment.^{20–22} BOD1L1-deficient cells display small spindles with kinetochores located close to the poles, whereas late-prometaphase cells had difficulties in chromosome alignment (Figures 2E and 2F), with many chromosomes located proximal to the spindle poles. Mitotic delay in BOD1L1-deficient cells was confirmed using time-lapse microscopy (Figures 2G and S4A) demonstrating that BOD1L1 is required for efficient mitotic progression. Finally, quantifying spindle microtubule intensity following cold treatment, we showed that spindle microtubule intensity in BOD1L1-deficient cells was increased in both prometaphase and metaphase relative to cells transfected with control shRNA (Figures S4B and S4C).

Using immunofluorescence microscopy, we detected BOD1L1 at spindle poles, on microtubules, and at a subset of kinetochores of SW620 cells (Figures 3A and 3B). Line scans showed significant overlap between BOD1L1 and Hec1 at kinetochores in prometaphase through anaphase. There was also a large degree of co-localization between AurKA and BOD1L1 at the spindle poles and along pole-proximal microtubules (Figure 3C). BOD1L1 co-localized with Hec1 on kinetochores in cells treated with either a low or high dose of nocodazole, demonstrating that BOD1L1 does not require microtubules for kinetochore localization (Figure S2E). BOD1L1 localization was not affected by inhibitors of AurKA or AurKB (Figure S2F). BOD1L1 localization was similar in RPE1 cells (Figures 3, S2B, S2D–S2F, and S3).

We next examined whether BOD1L1 affects AurKA signaling. The ratio of AurKA to pT288 AurKA remained unchanged in cells treated acutely with or adapted to UMK57 compared to control cells (i.e., no change in phospho-occupancy), although the overall levels of both AurKA and pT288 AurKA on mitotic spindles strongly increased in cells treated with UMK57 (Figures 4A and 4B). The level of TPX2²³ on the mitotic spindle in cells treated with UMK57 was also elevated despite a decrease in overall levels of spindle microtubules in treated cells (Figures 4C and

4E). TACC3, another spindle-associated protein, displayed spindle intensity that roughly mirrored the levels of spindle microtubules (Figures 4D and 4E), indicating that the quantity of AurKA and TPX2 on spindles selectively increased upon UMK57 treatment.

BOD1L1 interacts with the PP2A-B56 phosphatase and regulates kinetochore phosphorylation

To gain further insight into the role(s) of BOD1L1 in mitosis, we immunoprecipitated BOD1L1 from mitotic cells to determine the identity of interacting proteins (Figures 5A and S4D). We detected components of the PP2A-B56 phosphatase complex, including both PPP2R1A and PPP2R1B regulatory subunits, the PPP2CA catalytic subunit, and the PPP2R5E epsilon adaptor subunit (Figure 5B; Table S3). This interaction was independently validated by immunoprecipitation/immunoblot (Figure 5C). A notable difference in the interactomes of BOD1 and BOD1L1²² is Hec1. We did not detect a change in BOD1L1 localization at kinetochores in HeLa cells with doxycycline-inducible CRISPR-Cas9 Hec1 genetic knockout²⁴ (Figure S4E).

Pull-down experiments using fragments of BOD1L1 fused to GST indicate that the region of BOD1L1 that bound to the PP2A complex most strongly was the uncharacterized central domain from amino acids 500–2,001 despite the high degree of similarity between the N terminus of BOD1L1 and Bod1. Additionally, the C-terminal F6 fragment also interacted with the PP2A B56 delta subunit (Figure 5D). In contrast, it is the N terminal F1–F2 Bod1-similar and C-terminal F6 regions that bind Rif1 in the context of the DNA damage response.¹⁶ Pairwise interaction simulations using AlphaFold software with each BOD1L1 fragment and PP2A complex component that bound in the glutathione S-transferase (GST) pull-down offers a compelling model for BOD1L1 F6 fragment binding to the PP2A B56 delta subunit. The basic stretches of amino acids in the C terminus of BOD1L1 bind to the previously characterized acidic patch present on all B56 subunits (Figure 5E). This acidic patch is critical for the ability of a subset of PP2A substrates to bind to the phosphatase and be dephosphorylated.²⁵ Occupation of this acidic patch by BOD1L1 would prevent PP2A substrates from binding to the phosphatase. Moreover, these same basic stretches in BOD1L1 also form the recognition motifs for the AurKA phosphorylation sites we detected in the screen, suggesting that binding between the BOD1L1 C terminus and PP2A B56 subunits can be modulated by AurKA. Binding assays *in vitro* confirmed direct interaction of BOD1L1 F6 to PP2A B56 gamma (Figure S4F). Furthermore, using an *in vitro* phosphatase assay with an AurKA-phosphorylated fragment

Figure 3. BOD1L1 localizes to the mitotic spindle and kinetochores

- (A) Immunofluorescence images from SW620 cells in various stages of mitosis stained for BOD1L1, Hec1, and DAPI. The BOD1L1 and Hec1 channels were adjusted evenly for brightness and contrast. The DAPI channel of each condition was adjusted independently. Representative images from 2 independent biological experiments are shown. Scale bars, 10 μm and 1 μm (inset). Line scans across the indicated pairs of kinetochores are shown.
- (B) Immunofluorescence images from SW620 cells in various stages of mitosis stained for BOD1L1, α-tubulin, and DAPI. The BOD1L1 and α-tubulin channels were adjusted evenly for brightness and contrast. The DAPI channel of each condition was adjusted independently. Representative images from 2 independent biological experiments are shown. Scale bars, 10 μm and 1 μm (inset). Line scans across the indicated region of the mitotic spindle are shown.
- (C) Immunofluorescence images from SW620 cells in various stages of mitosis stained for BOD1L1, Aurora A, and DAPI. The BOD1L1 and Hec1 channels were adjusted evenly for brightness and contrast. The DAPI channel of each condition was adjusted independently. Representative images from 2 independent biological experiments are shown. Scale bars, 10 μm and 1 μm (inset). Line scans across the indicated region of the mitotic spindle are shown.

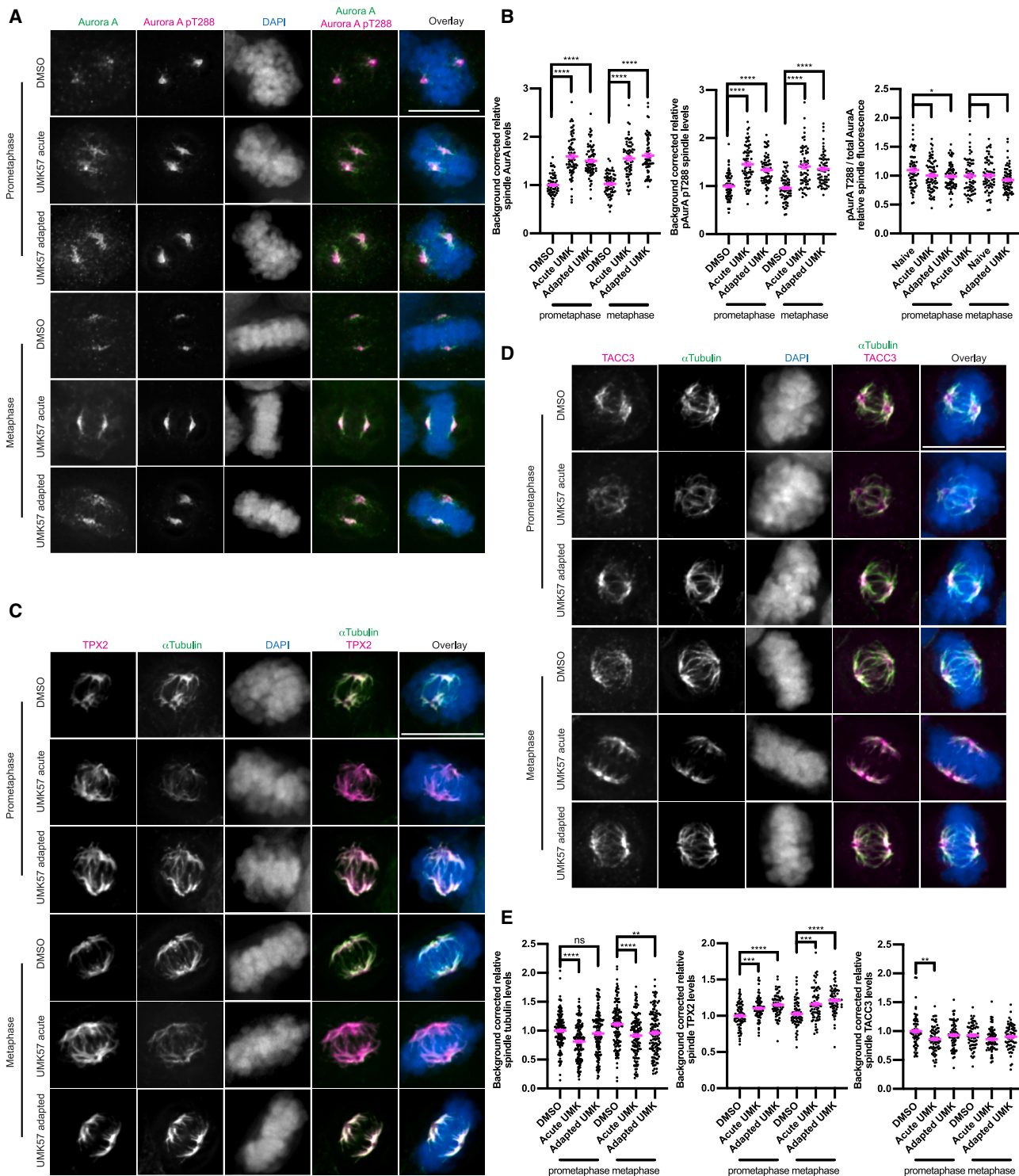


Figure 4. Microtubule destabilization mediated by hyperactive MCAK enhances Aurora A/TPX2 localization to mitotic spindles

(A) Immunofluorescence images from SW620 cells treated either with DMSO control, acutely (1 h) with UMK57, or with UMK57 for 3 days. The cells were then fixed and stained for total Aurora A and Aurora A pT288. Aurora A and Aurora A pT288 were adjusted evenly for brightness and contrast. The DAPI channel of each condition was adjusted independently. Representative images from 2 independent biological experiments are shown. Scale bars, 10 μ m.

(legend continued on next page)

of Kif4A as an idealized substrate of PP2A, we observed dephosphorylation of both AurKA and Kif4 by PP2A. In the presence of the GST-BOD1L1 F6 fragment, the rate of dephosphorylation of Kif4A and AurKA was reduced, showing that BOD1L1 can block PP2A phosphatase activity *in vitro* (Figures 5F and S4G).

To assess potential BOD1L1 regulation of the PP2A-B56 complex during mitosis, we quantified the staining intensity for numerous phosphorylated proteins at kinetochores following depletion of BOD1L1, including AurKA pT288 (AurKA), Hec1 pS55 (AurKA), Hec1 pT31 (Cdk1-Cyclin B1), Hec1 pS44 (AurKB), Dsn1 pS100 (AurKB), Knl1 pMELT (Mps1), AurKB pT232 (AurKB), and MCAK pS95 (AurKB). We observed that the intensity of staining for Hec1 pS55, Hec1 pT31, Hec1 pS44, pDsn1 pS100, and Knl1 pMELT decreased in both prometaphase and metaphase and that AurKB pT232 levels decreased in prometaphase in BOD1L1-deficient cells. In contrast, MCAK pS95 staining intensity increased in metaphase cells (Figure 6). We did not detect changes for AurKA pT288, indicating that total AurKA activity levels are essentially unchanged in BOD1L1-deficient mitotic cells. To verify that the observed changes in kinetochore protein phosphorylation were directly caused by loss of BOD1L1, we transfected SW620 BOD1L1 knockdown cells with a plasmid to express GFP-BOD1L1 and quantified the level of Hec1-pT31 and KNL1-pMELT. The expression of GFP-BOD1L1 restored Hec1 and KNL1 phosphorylation levels in the knockdown cells and slightly increased the relative phosphorylation levels compared to control cells (Figures S5A–S5C, S5F, and S5G). Similar results were observed following knockdown of BOD1L1 in the non-transformed, diploid cell line RPE1 (Figures S5D, S5E, S5H, and S5I). Thus, BOD1L1 functions as a negative regulator of protein phosphatase activity during mitosis.

The *BOD1L1* gene is mutated in human cancers

Since aneuploidy is associated with cancer development, and BOD1L1-deficiency increases mitotic error rates, we examined whether BOD1L1 is mutated in human cancers. The Cancer Genome Atlas (TCGA) for cancers shows somatic alterations in the wild-type sequence in *BOD1L1*. Among the 10,967 cancers that have been sequenced, 3.9% show alterations in the *BOD1L1* sequence. The five cancers with the highest percentage of *BOD1L1* somatic alterations are uterine endometrial carcinoma (12.9%), lung adenocarcinoma (8.8%), skin cutaneous melanoma (7.9%), stomach adenocarcinoma (7.7%), and lung squamous cell carcinoma (6.6%) (Figure 7A). Because our data demonstrate that BOD1L1 is activated by AurKA and functionally regulates PP2A activity, we also examined the TCGA for cancers that have alterations in any of the genes of the AurKA-BOD1L1-PP2A axis. Surprisingly, 59.6% of uterine carcinosarcoma and

43.9% of uterine endometrial cancers have alterations in one or more of these genes, suggesting that genes in this biochemical pathway might be particularly relevant in these cancer types (Figure S6A). We next tested associations of *BOD1L1* alteration with 5-year overall survival, adjusting for potential confounders in these patients. *BOD1L1* alteration was significantly associated with improved 5-year survival in uterine cancer (HR [hazard ratio] = 0.37 [95% confidence interval (CI): 0.16–0.85]) and reduced 5-year survival in lung adenocarcinoma (HR = 1.66 [95% CI: 1.03–2.66]) and melanoma (HR = 1.79 [95% CI: 1.07–3.00]). *BOD1L1* alteration did not demonstrate a significant association with patient survival in stomach adenocarcinoma or lung squamous cell carcinoma (Figure 7B). Using data from the TCGA-PanCancer Atlas ($n = 10,967$), we observed that *BOD1L1* alterations were exclusive of alterations to other *AURKA-BOD1L1-PP2A* gene pathway members. This was true when testing *BOD1L1* alteration versus alteration to any other gene pathway member (Fisher's exact test, $p = 1.3E-24$) and *BOD1L1* alteration versus each of the 11 gene pathway members independently (all Fisher's exact test, $p < 5.7E-08$) (Figures S6B and S6C), suggesting that mutations in multiple components of this pathway are not tolerated in cancers.

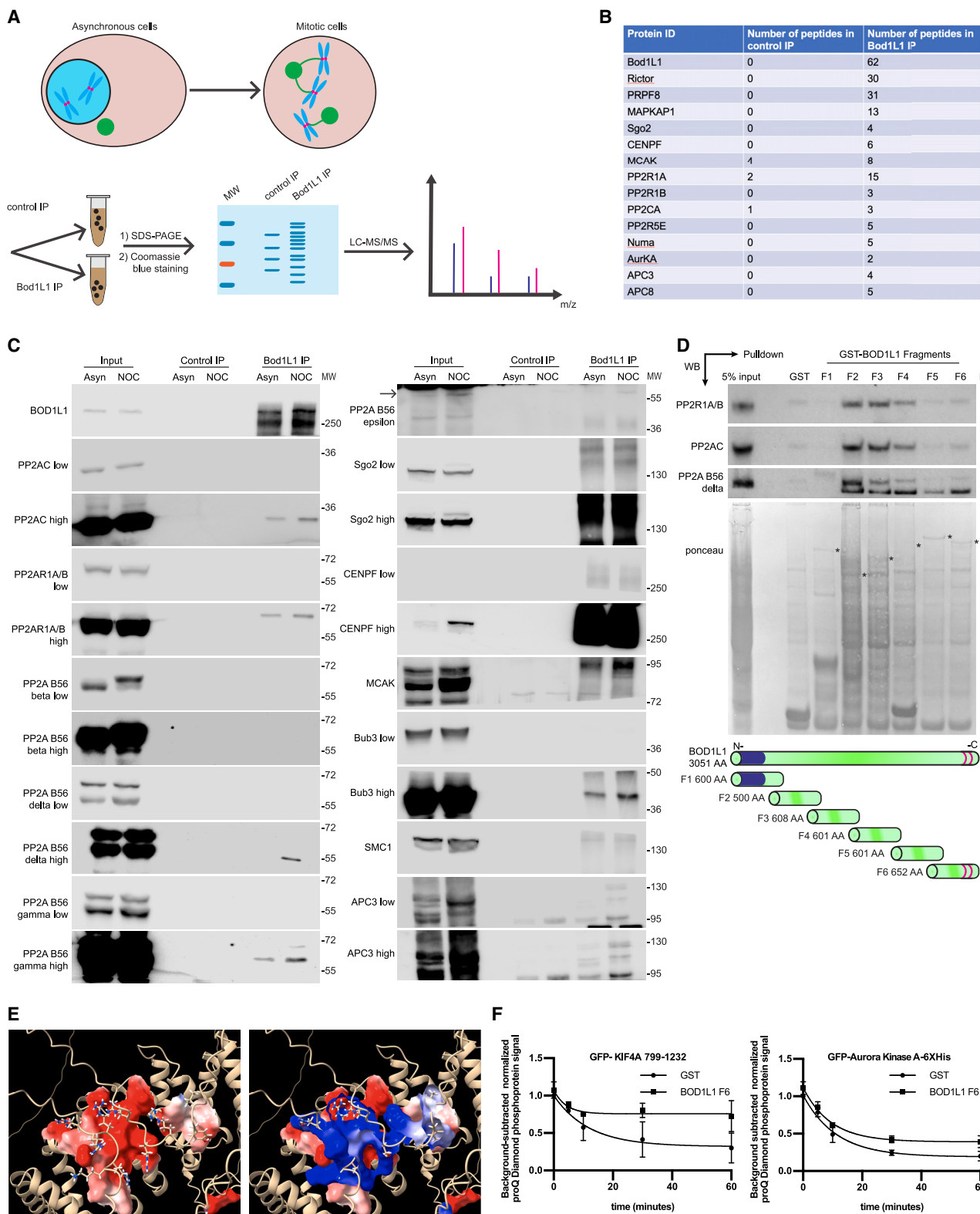
To understand how BOD1L1 inactivation affects cell proliferation and response to anti-mitotic drugs, including AurKA inhibitors or Taxol, we compared the proliferation of cells derived from various tumor types (U2OS [osteosarcoma], HCT116 [colorectal carcinoma], SW620 [colorectal adenocarcinoma], HeLa [cervical adenocarcinoma], and HEC1 [uterine endometrial adenocarcinoma]) following transfection with either control shRNA or BOD1L1-specific shRNA. All of these cell lines express BOD1L1, albeit at different levels, and they all displayed a significant increase in lagging chromosome rates following depletion of BOD1L1 (Figures S6D and S6E). All cell types tested had reduced proliferation following transfection with the BOD1L1-specific shRNA compared to the control shRNA, although the magnitude of the reduction varied between cell types. This variance was not proportional to the level of BOD1L1 expression (e.g., HEC1 and SW620 cells had comparable expression but different BOD1L1 sensitivities) (Figures 7C, 7D, S6D, and S6G). The impact of BOD1L1 deficiency on the response to treatment with Taxol and the AurKA inhibitor also varied among cell lines (Figures 7C, 7D, and S6G). In line with the differential toxicity we observed, U2OS cells with BOD1L1 knockdown formed micronuclei at a higher rate compared to control cells, while in SW620 cells, there was no difference in micronucleus formation between control and BOD1L1 knockdown conditions (Figure S6F). Thus, the relative impact of BOD1L1 gene alteration on patient cancer survival is variable, which is mirrored by a variable impact on proliferation of various cancer cell types

(B) Quantification of the relative spindle protein intensities from the conditions from (A). The levels of the prometaphase DMSO conditions was set to 1, and the other conditions shown as fold changes. The fluorescence levels for at least 30 cells for each of 2 independent biological repeats were measured. Error bars indicate the mean \pm SEM. Statistical significance was calculated between the indicated conditions using Dunnett's multiple-comparisons test. * $p < 0.05$, ** $p < 0.01$, *** $p < 0.001$.

(C) Cells were prepared as for (A) but stained for TPX2 and α -tubulin.

(D) Cells were prepared as for (A) but stained for TACC3 and tubulin.

(E) Quantification of the relative spindle protein intensities from (C) and (D). The tubulin intensities from (C) and (D) were combined into a single plot. * $p < 0.05$, ** $p < 0.01$, *** $p < 0.001$, **** $p < 0.0001$.



(legend on next page)

following BOD1L1 depletion. In RPE1 cells, immunoblots verify that the knockdown of BOD1L1 with each shRNA sequence was efficient (Figure S7A), although this did not sensitize RPE1 cells to Taxol or the AurKA inhibitor at the dosages used (Figures S7B and S7C).

DISCUSSION

Using an unbiased proteomics screen, we discovered a pathway that regulates mitotic fidelity by controlling phosphatase activity directed at kinetochore substrates. In unperturbed mitosis, BOD1L1 binds and inhibits PP2A-B56, helping to maintain moderate levels of phosphorylation of kinetochore substrates, thus decreasing K-MT attachment stability and ultimately supporting mitotic progression and fidelity. When CIN cancer cells are treated for prolonged periods with UMK57 to destabilize K-MT attachments, the adaptation response involves increased recruitment of AurKA to spindles through TPX2, which increases phosphorylation of BOD1L1 and relieves the negative regulation of PP2A activity. Relief of this constraint on PP2A leads to reduced phosphorylation of kinetochore substrates at the K-MT interface, which restores hyperstable K-MT stability and resumes the CIN phenotype (Figure 7E). This mechanism for adaptation to UMK57 is consistent with the broad decrease in phosphorylation in our phosphoproteomics dataset in cells adapted to UMK57, with data showing that small changes in kinetochore phosphorylation can cause large changes in chromosome segregation fidelity^{26–28} and that the mechanism of adaptation is independent of the continued functional impact of UMK57 to activate MCAK.¹¹

Consistently, the gene cell proliferation-regulating inhibitor of protein phosphatase 2A (*CIP2A*) is fourth on the list of *BOD1L1* co-dependent genes from the Cancer Dependency Map Project.^{29,30} *CIP2A* is a functional oncogene that inhibits the PP2A complex during the DNA damage response, mitotic entry, and mitotic progression by replacing the structural subunit of the PP2A complex, blocking phosphatase function.^{31,32} This co-dependency suggests that cell lines do not tolerate the loss of multiple negative regulators of PP2A activity.

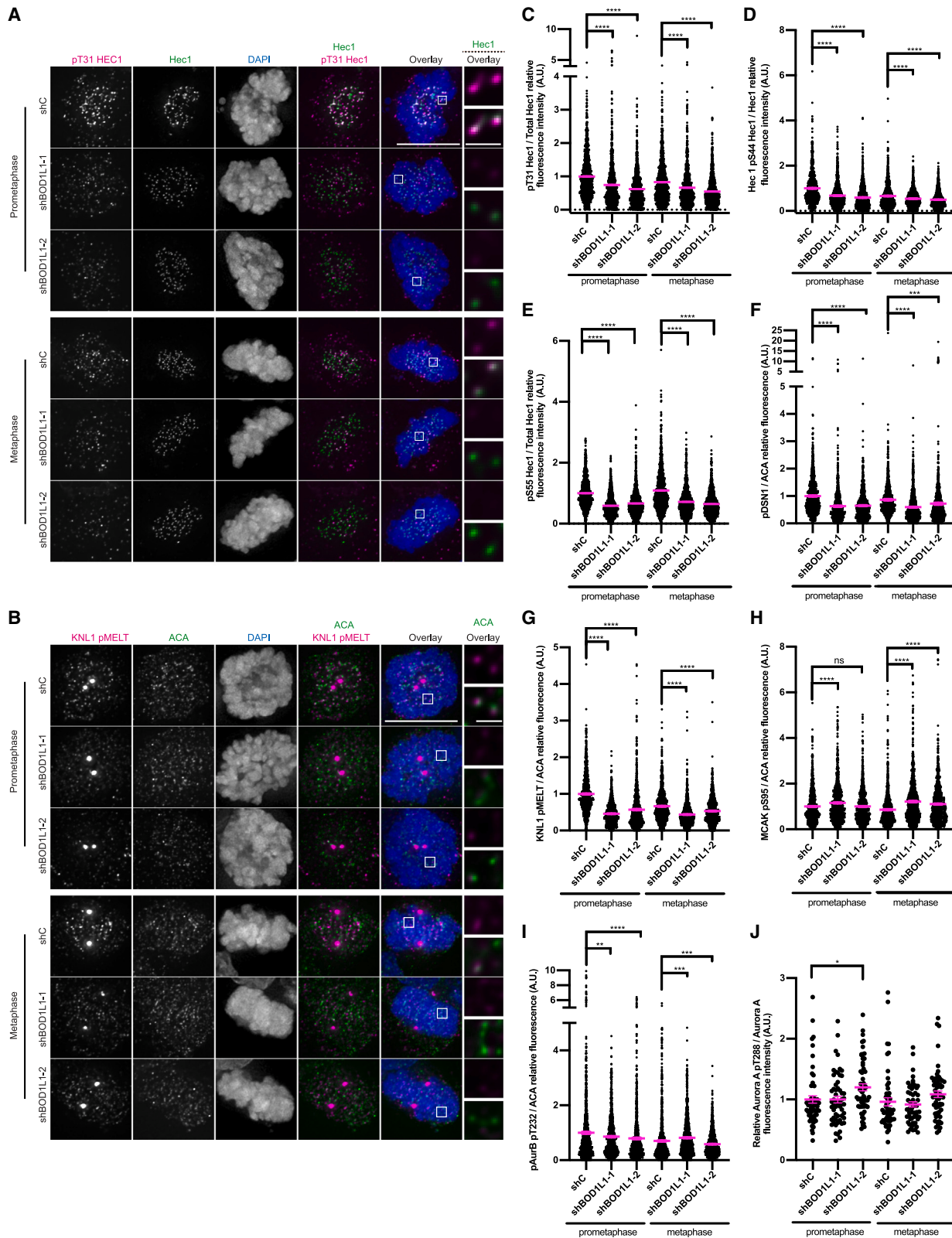
AurKA and AurKB effect mitotic fidelity by phosphorylation of spindle-associated and kinetochore substrates.^{27,33–35} Our

data demonstrate that AurKA regulates kinetochore substrate phosphorylation through regulation of BOD1L1 as a negative regulator of PP2A and that this role of AurKA is responsible for changes in K-MT attachment stability induced by a prolonged increase in MCAK activity caused by UMK57 treatment. In this context, an intriguing possibility emerges: the AurKA-BOD1L1-PP2A axis identified in this work is activated by hypostable K-MT attachments (or hypostable spindle MTs more broadly) and induces a compensating increase in K-MT stability. Conversely, AurKB has a well-recognized role in decreasing K-MT stability. Together, overall spindle MT stability and/or density would be established through a lower bound regulated by AurKA activity and an upper bound regulated by AurKB activity. In support of this idea, TPX2 may serve as a sensor of MT stability to marshal AurKA as needed because TPX2 has been shown to sense and influence the conformational state of microtubules³⁶ while promoting MT assembly by suppressing tubulin subunit off rates.³⁷ Moreover, this role of AurKA in stabilizing spindle microtubules through BOD1L1 is consistent with many tumor cells overexpressing or having hyperactive AurKA^{38–40} and also having CIN as a consequence of hyperstable K-MT attachments. Our observations suggest that AurKA may influence K-MT attachment stability through direct kinetochore substrate phosphorylation or through indirect regulation of PP2A activity.

Importantly, we found that the gene encoding BOD1L1 is occasionally altered in human cancers (Figure 7A). The functional consequence of these alterations remains unknown, although it is likely that some of them cause a loss of function. Thus, a reduced likelihood of death in uterine endometrial cancer would be consistent with our findings that BOD1L1 knockdown results in loss of fitness of various tumor lines and vulnerability to Taxol or an AurKA inhibitor (Figures 7C and 7D), which is corroborated by the mitotic arrest and occasional mitotic catastrophe observed in cells with BOD1L1 knockdown even in the absence of these drugs (Figures 2G and S4A). Since BOD1L1 also plays a role in the cellular response to DNA replication stress and DNA repair,^{16,18} these alterations may also contribute to the loss of fitness through that role. In contrast to patients with uterine endometrial cancer, alterations in BOD1L1 were associated with an increased risk of death in lung adenocarcinoma and in

Figure 5. BOD1L1 interacts with the PP2A-B56 phosphatase complex

- (A) Experimental schematic to identify BOD1L1-interacting proteins. SW620 cells were synchronized, and BOD1L1 was then immunoprecipitated and purified along with interacting proteins. The samples were then separated by SDS-PAGE. The entire lanes were excised, cut into 5 pieces, and analyzed by mass spectrometry. The experiment was performed once.
- (B) Selected interacting proteins detected in the control immunoprecipitation and BOD1L1 immunoprecipitations showing the number of detected peptides.
- (C) SW620 cells were prepared as in (A), except that they were analyzed by western blot. BOD1L1 was immunoprecipitated, and the purified proteins were then separated by SDS-PAGE, transferred to a nitrocellulose membrane, and blotted as indicated. The panels were adjusted for brightness and contrast. An experiment representative of two independent biological repeats is shown.
- (D) SW620 mitotic nuclear cell extracts were incubated with GST or GST-BOD1L fragments. Complexes were then isolated by glutathione Sepharose and analyzed by western blot. The blot shown is representative of 2 independent experiments.
- (E) AlphaFold Multimer model of BOD1L1 F6 bound to PPP2R5D, showing the acidic patch on PPP2R5D in red and the basic stretches of BOD1L1 in blue.
- (F) HEK293T cells were transfected with 3×FLAG-PPP2R5C or empty vector. 48 h following transfection, the cells were harvested and lysed. 3×FLAG-PPP2R5C was then purified by immunoprecipitation. GST control or BOD1L1 F6 was then added, along with GFP-KIF4A 799–1,232 phosphorylated *in vitro* by GFP-His-Aurora A. The samples were then incubated at 37°C until the reaction was stopped by addition of 4× sample buffer. The reaction was then run on SDS-PAGE gel, which was then stained with ProQ-Diamond, imaged, stained with Coomassie, and re-imaged. Band intensities were measured using Fiji using an adjacent empty lane for background intensity, which was subtracted. The band intensities were then normalized and plotted. Three independent biological experiments were performed, and the data from each time point were averaged. A one-phase exponential decay curve was then fitted to the data.



(legend on next page)

skin cutaneous melanoma. The clinically differing impacts of BOD1L1 alteration might depend on whether it is the mitotic functions and/or DNA repair functions that have been altered relative to the alterations at the root of a specific type of cancer. For example, both lung adenocarcinoma (if caused by smoking) and skin melanoma are driven by DNA damage caused by chemicals or UV light, thus highlighting the role of BOD1L1 in DNA repair, whereas in endometrial cancer, the cyclic high proliferation rate of this tissue in women of reproductive age might highlight the role of BOD1L1 in maintaining accurate mitosis.

Limitations of the study

Although we discovered a role of BOD1L1 in regulating the mitotic spindle and cell division through the PP2A-B56 phosphatase, we were unable to discover whether BOD1L1 binds directly to microtubules or whether there is an intermediate receptor that enables BOD1L1 to localize to the spindle. Similarly, we have been unable to determine the kinetochore receptor for BOD1L1 and why BOD1L1 localizes only to a subset of kinetochores. It remains possible that the kinetochore receptor did not appear in our screen, and so an unbiased screening approach might be required to determine which proteins are necessary for BOD1L1 to localize to the spindle and kinetochore. Last, we also need to prove experimentally that phosphorylation of C-terminal sites by AurKA regulates the interaction between BOD1L1 and PP2A.

RESOURCE AVAILABILITY

Lead contact

Requests for further information, resources, and reagents should be directed to and will be fulfilled by the lead contact, Duane Compton (duane.a.compton@dartmouth.edu).

Materials availability

The plasmids created for this study are available from the [lead contact](#) upon request.

Data and code availability

- No new code was generated for this manuscript.
- The cell biology datasets generated and/or analyzed during the current study are available from the corresponding author upon reasonable request.

Figure 6. BOD1L1 expression is required for normal kinetochore phosphorylation

(A) Immunofluorescence images from SW620 cells transfected with control shRNA or shRNA against BOD1L1 in prometaphase or metaphase and stained for Hec1, Hec1 pT31, and DAPI. The BOD1L1 and Hec1 channels were adjusted evenly for brightness and contrast. The DAPI channel of each condition was adjusted independently. Representative images from 2 independent biological experiments are shown. Scale bars, 10 μm and 1 μm (inset).

(B) As for (A) except for KNL1 pMELT/ACA instead of Hec1 pT31/total Hec1.

(C) Quantification of the relative kinetochore pT31 Hec1/Hec1 intensities from the conditions from (A). The condition with the lowest level of pT31 Hec1/Hec1 was set to 1, and the other conditions are shown as fold changes. 25 kinetochores were quantified from each of 20 cells for each of 2 independent biological repeats. Error bars indicate the mean ± SEM. Statistical significance was calculated between the indicated conditions using Dunnett's multiple-comparison test. **p* < 0.05, ***p* < 0.01, ****p* < 0.001, *****p* < 0.0001.

(D) As for (C) except for Hec1 pS44/total Hec1 instead of Hec1 pT31/total Hec1.

(E) As for (C) except for Hec1 pS55/total Hec1 instead of Hec1 pT31/total Hec1.

(F) As for (C) except for DSN1 pS109/ACA instead of Hec1 pT31/total Hec1.

(G) As for (C) except for KNL1 pMELT/ACA instead of Hec1 pT31/total Hec1.

(H) As for (C) except for MCAK pS95/ACA instead of Hec1 pT31/total Hec1.

(I) As for (C) except for Aurora B pT232/ACA instead of Hec1 pT31/total Hec1.

(J) Quantification of total cellular Aurora A pT288/total Aurora A. The condition with the lowest level of pT31 Hec1/Hec1 was set to 1, and the other conditions are shown as fold changes. The level of protein was measured from at least 25 cells for each of 2 independent biological repeats. Error bars indicate the mean ± SEM. Statistical significance was calculated between the indicated conditions using Dunnett's multiple-comparisons test.

- The datasets for the total protein screen, phosphoproteomics screen, and BOD1L1 interactomes have been deposited into the ProteomeXchange Consortium via the PRIDE⁴¹ partner repository with the dataset identifiers PRIDE: PXD058821, PRIDE: PXD058823, and PRIDE: PXD058824.
- Any additional information required to reanalyze the data reported in this paper is available from the [lead contact](#) upon request.

ACKNOWLEDGMENTS

We thank Grant Stewart, Rebecca Page, Jakob Nilsson, Jennifer Delucca, Iain Cheeseman, Tyler Curiel, Jose Teodoro, and Adrian Saurin for providing reagents. We thank Sanjukta Guha Thakurta (Thermo Fisher Center for Multiplexed Proteomics, Harvard University) and Ross Tomaino (Taplin Mass Spectrometry Facility, Harvard University) for assistance with the proteomics analysis. We thank Arminja Kettenbach, Scott Gerber, and members of the Compton laboratory for helpful discussions. T.J.K. was supported by fellowships from the Fonds de Recherche du Québec – Santé and the Canadian Institutes of Health Research. The laboratory of S.B. is supported by grants from the Canadian Institutes of Health Research (CIHR PJT-189995), the Natural Sciences and Engineering Research Council of Canada (NSERC; RGPIN-2024-05603), and in part by a Fonds de recherche du Québec (Health Sector) Research Centres grant (288558). This work was also supported by a grant from the National Institutes of Health (GM051542 to D.A.C.). The authors acknowledge the following Shared Resources facilities (Bio-Rad ChemiDoc MP) at the Norris Cotton Cancer Center at Dartmouth with NCI Cancer Center Support Grant 5P30 CA023108-40.

AUTHOR CONTRIBUTIONS

Conceptualization, D.A.C. and T.J.K.; investigation, T.J.K., I.M.V., T.L., and M.R.H.; formal analysis, T.J.K. and I.M.V.; methodology, T.J.K. and D.A.C.; funding acquisition, T.J.K. and D.A.C.; supervision, B.C.C., S.B., and D.A.C.; writing – original draft, T.J.K.; writing – review & editing, T.J.K., M.R.H., B.C.C., and D.A.C.; project administration, D.A.C.

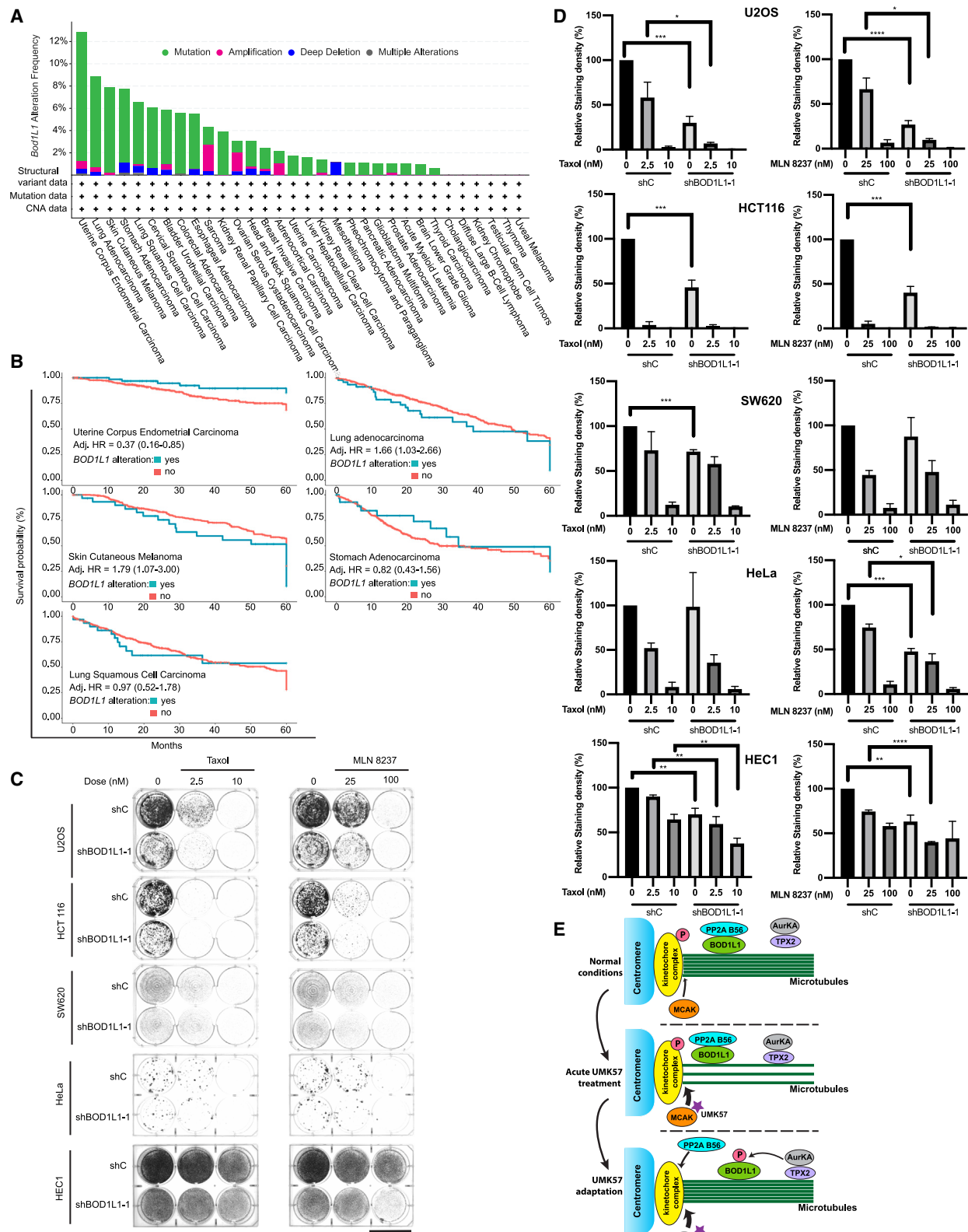
DECLARATION OF INTERESTS

The authors declare no competing interests.

STAR METHODS

Detailed methods are provided in the online version of this paper and include the following:

- KEY RESOURCES TABLE
- EXPERIMENTAL MODEL AND STUDY PARTICIPANT DETAILS



(legend on next page)

● **METHOD DETAILS**

- Inhibitors and reagents
- Plasmids and cloning
- Proteomic screens
- Whole proteome profiling
- Transfections
- SDS-PAGE and western blot
- Immunoprecipitation
- Identification of BOD1L1 interacting proteins
- RNA interference
- Immunofluorescence
- *In vitro* analysis of BOD1L1
- *In vitro* phosphatase reaction
- Microscopy
- Antibodies

● **QUANTIFICATION AND STATISTICAL ANALYSIS**

- Statistical analysis of cell biology data
- Population data, and statistical analysis

SUPPLEMENTAL INFORMATION

Supplemental information can be found online at <https://doi.org/10.1016/j.celrep.2025.115317>.

Received: August 11, 2023

Revised: November 24, 2024

Accepted: January 23, 2025

Published: February 18, 2025

REFERENCES

1. Luo, J., Solimini, N.L., and Elledge, S.J. (2009). Principles of Cancer Therapy: Oncogene and Non-oncogene Addiction. *Cell* 136, 823–837. <https://doi.org/10.1016/j.cell.2009.02.024>.
2. Geigl, J.B., Obenauf, A.C., Schwarzenbach, T., and Speicher, M.R. (2008). Defining 'chromosomal instability'. *Trends Genet.* 24, 64–69. <https://doi.org/10.1016/j.tig.2007.11.006>.
3. Lengauer, C., Kinzler, K.W., and Vogelstein, B. (1997). Genetic instability in colorectal cancers. *Nature* 386, 623–627. <https://doi.org/10.1038/386623a0>.
4. Thompson, S.L., and Compton, D.A. (2011). Chromosome missegregation in human cells arises through specific types of kinetochore-microtubule attachment errors. *Proc. Natl. Acad. Sci. USA* 108, 17974–17978. <https://doi.org/10.1073/pnas.1109720108>.
5. Bakhour, S.F., Thompson, S.L., Manning, A.L., and Compton, D.A. (2009). Genome stability is ensured by temporal control of kinetochore-microtubule dynamics. *Nat. Cell Biol.* 11, 27–35. <https://doi.org/10.1038/ncb1809>.
6. Kleyman, M., Kabeche, L., and Compton, D.A. (2014). STAG2 promotes error correction in mitosis by regulating kinetochore-microtubule attachments. *J. Cell Sci.* 127, 4225–4233. <https://doi.org/10.1242/jcs.151613>.
7. Bakhour, S.F., Genovese, G., and Compton, D.A. (2009). Deviant Kinetochore Microtubule Dynamics Underlie Chromosomal Instability. *Curr. Biol.* 19, 1937–1942. <https://doi.org/10.1016/j.cub.2009.09.055>.
8. Bakhour, S.F., Kabeche, L., Murnane, J.P., Zaki, B.I., and Compton, D.A. (2014). DNA-Damage Response during Mitosis Induces Whole-Chromosome Misseggregation. *Cancer Discov.* 4, 1281–1289. <https://doi.org/10.1158/2159-8290.CD-14-0403>.
9. Hunter, A.W., Caplow, M., Coy, D.L., Hancock, W.O., Diez, S., Wordeman, L., and Howard, J. (2003). The Kinesin-Related Protein MCAK Is a Microtubule Depolymerase that Forms an ATP-Hydrolyzing Complex at Microtubule Ends. *Mol. Cell* 11, 445–457. [https://doi.org/10.1016/S1097-2765\(03\)00049-2](https://doi.org/10.1016/S1097-2765(03)00049-2).
10. Maney, T., Hunter, A.W., Wagenbach, M., and Wordeman, L. (1998). Mitotic Centromere-associated Kinesin Is Important for Anaphase Chromosome Segregation. *J. Cell Biol.* 142, 787–801. <https://doi.org/10.1083/jcb.142.3.787>.
11. Orr, B., Talje, L., Liu, Z., Kwok, B.H., and Compton, D.A. (2016). Adaptive Resistance to an Inhibitor of Chromosomal Instability in Human Cancer Cells. *Cell Rep.* 17, 1755–1763. <https://doi.org/10.1016/j.celrep.2016.10.030>.
12. Kettenbach, A.N., Schewpke, D.K., Faherty, B.K., Pechenick, D., Pletnev, A.A., and Gerber, S.A. (2011). Quantitative Phosphoproteomics Identifies Substrates and Functional Modules of Aurora and Polo-Like Kinase Activities in Mitotic Cells. *Sci. Signal.* 4, rs5. <https://doi.org/10.1126/scisignal.2001497>.
13. Huang, H., Feng, J., Famulski, J., Rattner, J.B., Liu, S.T., Kao, G.D., Muschel, R., Chan, G.K.T., and Yen, T.J. (2007). Tripin/hSgo2 recruits MCAK to the inner centromere to correct defective kinetochore attachments. *J. Cell Biol.* 177, 413–424. <https://doi.org/10.1083/jcb.200701122>.
14. Tanno, Y., Kitajima, T.S., Honda, T., Ando, Y., Ishiguro, K.I., and Watanabe, Y. (2010). Phosphorylation of mammalian Sgo2 by Aurora B recruits PP2A and MCAK to centromeres. *Genes Dev.* 24, 2169–2179. <https://doi.org/10.1101/gad.1945310>.
15. Arslanhan, M.D., Rauniyar, N., Yates, J.R., and Firat-Karalar, E.N. (2021). Aurora Kinase A proximity map reveals centriolar satellites as regulators of its ciliary function. *EMBO Rep.* 22, e51902. <https://doi.org/10.15252/embr.202051902>.
16. Bayley, R., Borel, V., Moss, R.J., Sweatman, E., Ruis, P., Ormrod, A., Goula, A., Mottram, R.M.A., Staniage, T., Hewitt, G., et al. (2022). H3K4 methylation by SETD1A/BOD1L facilitates RIF1-dependent NHEJ. *Mol. Cell* 82, 1924–1939.e10. <https://doi.org/10.1016/j.molcel.2022.03.030>.
17. Moustafa-Kamal, M., Gamache, I., Lu, Y., Li, S., and Teodoro, J.G. (2013). BimEL is phosphorylated at mitosis by Aurora A and targeted for degradation by β TrCP1. *Cell Death Differ.* 20, 1393–1403. <https://doi.org/10.1038/cdd.2013.93>.
18. Higgs, M.R., Reynolds, J.J., Winczura, A., Blackford, A.N., Borel, V., Miller, E.S., Zlatanou, A., Niemuszczycy, J., Ryan, E.L., Davies, N.J., et al. (2015). BOD1L Is Required to Suppress deleterious Resection of Stressed

Figure 7. BOD1L1 is mutated in human cancers

- (A) The 10,967 sequenced cancers in the TCGA were queried for the presence of mutations in the *BOD1L1* gene and plotted by cancer subtype.
- (B) Kaplan-Meier 5-year overall survival by *BOD1L1* alteration status with Cox proportional hazard ratios and 95% CIs from models adjusted for potential confounders (age, sex [except uterine], and tumor grade or stage]: uterine corpus endometrial carcinoma TCGA-UCEC, $n = 529$; lung adenocarcinoma TCGA-LUAD, $n = 667$; cutaneous melanoma TCGA-SKCM, $n = 448$; stomach adenocarcinoma TCGA-STAD, $n = 440$; and lung squamous cell carcinoma TCGA-LUSC, $n = 487$.
- (C) U2OS, HCT116, SW620, and HeLa cells were then transfected with control shRNA or shRNA against *BOD1L1* and selected with puromycin in the presence of compounds as indicated. After 1 week of selection, the cells were fixed and stained with crystal violet. Representative images from 3 independent experiments are shown. Scale bar, 4 cm.
- (D) Quantification of cells from (C). The staining intensity of the cells was measured using Fiji and plotted. Error bars indicate the mean \pm SEM. Statistical significance was calculated between the indicated conditions using Student's t test. * $p < 0.05$, ** $p < 0.01$, *** $p < 0.001$, **** $p < 0.0001$.
- (E) Cartoon showing a mechanism for adaptation to UMK57. UMK57 agonizes MCAK, resulting in lower k-MT stability, which is sensed by AurKA. AurKA then phosphorylates *BOD1L1*, releasing PP2A to reduce phosphorylation of the NDC80 complex, resulting in higher k-MT stability.

- Replication Forks. *Mol. Cell* 59, 462–477. <https://doi.org/10.1016/j.molcel.2015.06.007>.
19. Higgs, M.R., Sato, K., Reynolds, J.J., Begum, S., Bayley, R., Goula, A., Vernet, A., Paquin, K.L., Skalnik, D.G., Kobayashi, W., et al. (2018). Histone Methylation by SETD1A Protects Nascent DNA through the Nucleosome Chaperone Activity of FANCD2. *Mol. Cell* 71, 25–41.e6. <https://doi.org/10.1016/j.molcel.2018.05.018>.
 20. Porter, I.M., McClelland, S.E., Khoudoli, G.A., Hunter, C.J., Andersen, J.S., McAlpin, A.D., Blow, J.J., and Swedlow, J.R. (2007). Bod1, a novel kinetochore protein required for chromosome biorientation. *J. Cell Biol.* 179, 187–197. <https://doi.org/10.1083/jcb.200704098>.
 21. Porter, I.M., Schleicher, K., Porter, M., and Swedlow, J.R. (2013). Bod1 regulates protein phosphatase 2A at mitotic kinetochores. *Nat. Commun.* 4, 2677. <https://doi.org/10.1038/ncomms3677>.
 22. Schleicher, K., Porter, M., Sundaramoorthy, R., Porter, I.M., and Swedlow, J.R. (2017). The Ndc80 complex targets Bod1 to human mitotic kinetochores. *Open Biology* 7, 170099.
 23. Kufer, T.A., Silljé, H.H.W., Körner, R., Gruss, O.J., Meraldi, P., and Nigg, E.A. (2002). Human TPX2 is required for targeting Aurora-A kinase to the spindle. *J. Cell Biol.* 158, 617–623. <https://doi.org/10.1083/jcb.200204155>.
 24. McKinley, K.L., and Cheeseman, I.M. (2017). Large-Scale Analysis of CRISPR/Cas9 Cell-Cycle Knockouts Reveals the Diversity of p53-Dependent Responses to Cell-Cycle Defects. *Dev. Cell* 40, 405–420.e2. <https://doi.org/10.1016/j.devcel.2017.01.012>.
 25. Wang, X., Garvanska, D.H., Nasa, I., Ueki, Y., Zhang, G., Kettenbach, A.N., Peti, W., Nilsson, J., and Page, R. (2020). A dynamic charge-charge interaction modulates PP2A:B56 substrate recruitment. *Elife* 9, e55966. <https://doi.org/10.7554/elife.55966>.
 26. Kucharski, T.J. (2022). Chromosome segregation fidelity is controlled by small changes in phospho-occupancy at the kinetochore-microtubule interface. *J. Cell Biol.* 221, e202107107.
 27. Sobajima, T., Kowalczyk, K.M., Skylakakis, S., Hayward, D., Fulcher, L.J., Neary, C., Batley, C., Kurlekar, S., Roberts, E., Gruneberg, U., and Barr, F.A. (2023). PP6 regulation of Aurora A–TPX2 limits NDC80 phosphorylation and mitotic spindle size. *J. Cell Biol.* 222, e202205117. <https://doi.org/10.1083/jcb.202205117>.
 28. Zaytsev, A.V., Mick, J.E., Maslennikov, E., Nikashin, B., DeLuca, J.G., and Grishchuk, E.L. (2015). Multisite phosphorylation of the NDC80 complex gradually tunes its microtubule-binding affinity. *Mol. Biol. Cell* 26, 1829–1844. <https://doi.org/10.1091/mbc.E14-11-1539>.
 29. Meyers, R.M., Bryan, J.G., McFarland, J.M., Weir, B.A., Sizemore, A.E., Xu, H., Dharia, N.V., Montgomery, P.G., Cowley, G.S., Pantel, S., et al. (2018). Computational correction of copy-number effect improves specificity of CRISPR-Cas9 essentiality screens in cancer cells. *Nature genetics* 49, 1779–1784.
 30. Dempster, J.M., Rossen, J., Kazachkova, M., Pan, J., Kugener, G., Root, D.E., and Tsherniak, A. (2019). Extracting Biological Insights from the Project Achilles Genome-Scale CRISPR Screens in Cancer Cell Lines. *bioRxiv*, 720243. <https://doi.org/10.1101/720243>.
 31. Nagelli, S., and Westerman, J. (2024). CIP2A coordinates phospho-signaling, mitosis, and the DNA damage response. *Trends Cancer* 10, 52–64. <https://doi.org/10.1016/j.trecan.2023.09.001>.
 32. Pavic, K., Gupta, N., Omella, J.D., Derua, R., Aakula, A., Huhtaniemi, R., Määttä, J.A., Höfflin, N., Okkeri, J., Wang, Z., et al. (2023). Structural mechanism for inhibition of PP2A-B56 ζ and oncogenicity by CIP2A. *Nat. Commun.* 14, 1143. <https://doi.org/10.1038/s41467-023-36693-9>.
 33. DeLuca, K.F., Meppelink, A., Broad, A.J., Mick, J.E., Peersen, O.B., Pektaş, S., Lens, S.M.A., and DeLuca, J.G. (2018). Aurora A kinase phosphorylates Hec1 to regulate metaphase kinetochore–microtubule dynamics. *J. Cell Biol.* 217, 163–177. <https://doi.org/10.1083/jcb.201707160>.
 34. Ye, A.A., Deretic, J., Hoel, C.M., Hinman, A.W., Cimini, D., Welburn, J.P., and Maresca, T.J. (2015). Aurora A Kinase Contributes to a Pole-Based Er-
 - ror Correction Pathway. *Curr. Biol.* 25, 1842–1851. <https://doi.org/10.1016/j.cub.2015.06.021>.
 35. Campbell, C.S., and Desai, A. (2013). Tension sensing by Aurora B kinase is independent of survivin-based centromere localization. *Nature* 497, 118–121. <https://doi.org/10.1038/nature12057>.
 36. Zhang, R., Roostalu, J., Surrey, T., and Nogales, E. (2017). Structural insight into TPX2-stimulated microtubule assembly. *Elife* 6, e30959. <https://doi.org/10.7554/elife.30959>.
 37. Reid, T.A., Schuster, B.M., Mann, B.J., Balchand, S.K., Plooster, M., McClellan, M., Coombes, C.E., Wadsworth, P., and Gardner, M.K. (2016). Suppression of microtubule assembly kinetics by the mitotic protein TPX2. *J. Cell Sci.* 129, 1319–1328. <https://doi.org/10.1242/jcs.178806>.
 38. Bischoff, J.R., Anderson, L., Zhu, Y., Mossie, K., Ng, L., Souza, B., Schryver, B., Flanagan, P., Clairvoyant, F., Ginther, C., et al. (1998). A homologue of Drosophila aurora kinase is oncogenic and amplified in human colorectal cancers. *EMBO J.* 17, 3052–3065. <https://doi.org/10.1093/emboj/17.11.3052>.
 39. Zhou, H., Kuang, J., Zhong, L., Kuo, W.L., Gray, J.W., Sahin, A., Brinkley, B.R., and Sen, S. (1998). Tumour amplified kinase STK15/BTAK induces centrosome amplification, aneuploidy and transformation. *Nat. Genet.* 20, 189–193. <https://doi.org/10.1038/2496>.
 40. Sen, S., Zhou, H., and White, R.A. (1997). A putative serine/threonine kinase encoding gene BTAK on chromosome 20q13 is amplified and over-expressed in human breast cancer cell lines. *Oncogene* 14, 2195–2200.
 41. Perez-Riverol, Y., Bai, J., Bandla, C., García-Seisdedos, D., Hewapathirana, S., Kamatchinathan, S., Kundu, D.J., Prakash, A., Frericks-Zipper, A., Eisenacher, M., et al. (2022). The PRIDE database resources in 2022: a hub for mass spectrometry-based proteomics evidences. *Nucleic Acids Res.* 50, D543–D552. <https://doi.org/10.1093/nar/gkab1038>.
 42. DeLuca, K.F., Lens, S.M.A., and DeLuca, J.G. (2011). Temporal changes in Hec1 phosphorylation control kinetochore–microtubule attachment stability during mitosis. *J. Cell Sci.* 124, 622–634. <https://doi.org/10.1242/jcs.072629>.
 43. Welburn, J.P.I., Vleugel, M., Liu, D., Yates, J.R., Lampson, M.A., Fukagawa, T., and Cheeseman, I.M. (2010). Aurora B Phosphorylates Spatially Distinct Targets to Differentially Regulate the Kinetochore-Microtubule Interface. *Mol. Cell* 38, 383–392. <https://doi.org/10.1016/j.molcel.2010.02.034>.
 44. Gergely, F., Karlsson, C., Still, I., Cowell, J., Kilmartin, J., and Raff, J.W. (2000). The TACC domain identifies a family of centrosomal proteins that can interact with microtubules. *Proc. Natl. Acad. Sci. USA* 97, 14352–14357. <https://doi.org/10.1073/pnas.97.26.14352>.
 45. Moffat, J., Grueneberg, D.A., Yang, X., Kim, S.Y., Kloepfer, A.M., Hinkle, G., Piqani, B., Eisenhaure, T.M., Luo, B., Grenier, J.K., et al. (2006). A Lentiviral RNAi Library for Human and Mouse Genes Applied to an Arrayed Viral High-Content Screen. *Cell* 124, 1283–1298. <https://doi.org/10.1016/j.cell.2006.01.040>.
 46. Gee, P., Lung, M.S.Y., Okuzaki, Y., Sasakawa, N., Iguchi, T., Makita, Y., Hozumi, H., Miura, Y., Yang, L.F., Iwasaki, M., et al. (2020). Extracellular nanovesicles for packaging of CRISPR-Cas9 protein and sgRNA to induce therapeutic exon skipping. *Nat. Commun.* 11, 1334. <https://doi.org/10.1038/s41467-020-14957-y>.
 47. Stewart, S.A., Dykhoorn, D.M., Palliser, D., Mizuno, H., Yu, E.Y., An, D.S., Sabatini, D.M., Chen, I.S.Y., Hahn, W.C., Sharp, P.A., et al. (2003). Lentivirus-delivered stable gene silencing by RNAi in primary cells. *RNA* 9, 493–501. <https://doi.org/10.1261/rna.2192803>.
 48. Bertolin, G., Sizaire, F., Herbomel, G., Reboutier, D., Prigent, C., and Tramier, M. (2016). A FRET biosensor reveals spatiotemporal activation and functions of aurora kinase A in living cells. *Nat. Commun.* 7, 12674. <https://doi.org/10.1038/ncomms12674>.

49. Yates, J.R. (1994). An approach to correlate tandem mass spectral data of peptides with amino acid sequences in a protein database. *J. Am. Soc. Mass Spectrom.* 5, 976–989.
50. Schindelin, J., Arganda-Carreras, I., Frise, E., Kaynig, V., Longair, M., Pietzsch, T., Preibisch, S., Rueden, C., Saalfeld, S., Schmid, B., et al. (2012). Fiji: an open-source platform for biological-image analysis. *Nat. Methods* 9, 676–682. <https://doi.org/10.1038/nmeth.2019>.
51. R Core Team (2021). R: A Language and Environment for Statistical Computing (R Found. Stat. Comput.).
52. Therneau, T. (2024). A package for Survival Analysis in R. R package version 3.8-3. <https://CRAN.R-project.org/package=survival>.
53. Kassambara, A., Marcin K., Biecek, P., and Scheipl, F. (2024). Survminer: Drawing Survival Curves using “ggplot2.” <https://cran.r-project.org/web/packages/survminer/survminer.pdf>.
54. Navarrete-Perea, J., Yu, Q., Gygi, S.P., and Paulo, J.A. (2018). Streamlined Tandem Mass Tag (SL-TMT) Protocol: An Efficient Strategy for Quantitative (Phospho)proteome Profiling Using Tandem Mass Tag-Synchronous Precursor Selection-MS3. *J. Proteome Res.* 17, 2226–2236.
55. Li, J., Cai, Z., Bomgarden, R.D., Pike, I., Kuhn, K., Rogers, J.C., Roberts, T.M., Gygi, S.P., and Paulo, J.A. (2021). TMTpro-18plex: The Expanded and Complete Set of TMTpro Reagents for Sample Multiplexing. *J. Proteome Res.* 20, 2964–2972.
56. Elias, J.E., and Gygi, S.P. (2007). Target-decoy search strategy for increased confidence in large-scale protein identifications by mass spectrometry. *Nat. Methods* 4, 207–214. <https://doi.org/10.1038/nmeth1019>.
57. Rad, R., Li, J., Mintseris, J., O'Connell, J., Gygi, S.P., and Schweppe, D.K. (2021). Improved Monoisotopic Mass Estimation for Deeper Proteome Coverage. *J. Proteome Res.* 20, 591–598.
58. Huttlin, E.L. (2010). A Tissue-Specific Atlas of Mouse Protein Phosphorylation and Expression. *Cell* 143, 1174–1189.
59. Beausoleil, S.A., Villen, J., Gerber, S.A., Rush, J., and Gygi, S.P. (2006). A probability-based approach for high-throughput protein phosphorylation analysis and site localization. *Nat. Biotechnol.* 24, 1285–1292.
60. Kucharski, T.J., Minshall, P.E., Moustafa-Kamal, M., Turnell, A.S., and Teodoro, J.G. (2017). Reciprocal Regulation between 53BP1 and the Anaphase-Promoting Complex/Cyclosome Is Required for Genomic Stability during Mitotic Stress. *Cell Rep.* 18, 1982–1995. <https://doi.org/10.1016/j.celrep.2017.01.080>.
61. Shevchenko, A., Wilm, M., Vorm, O., and Mann, M. (1996). Mass Spectrometric Sequencing of Proteins from Silver-Stained Polyacrylamide Gels. *Anal. Chem.* 68, 850–858. <https://doi.org/10.1021/ac950914h>.
62. Peng, J., and Gygi, S.P. (2001). Proteomics: the move to mixtures. *J. Mass Spectrom.* 36, 1083–1091. <https://doi.org/10.1002/jms.229>.

STAR★METHODS

KEY RESOURCES TABLE

REAGENT or RESOURCE	SOURCE	IDENTIFIER
Antibodies		
human anti-ACA	Geisel School of Medicine	N/A
mouse anti-Hec1	Santa Cruz	Cat# sc-515550
mouse anti-PP2AR1A	Santa Cruz	Cat# SC-74580
mouse anti-PP2AC	Santa Cruz	Cat# SC-166034
rabbit anti-PP2A B56 Alpha	MyBioSource.com	Cat# MBS8524809
mouse anti-PP2A B56 Beta	Santa Cruz	Cat# sc-515676
mouse anti-PP2A B56 Gamma	Santa Cruz	Cat# sc-374379
mouse anti-PP2A B56 Delta	Santa Cruz	Cat# sc-271363
rabbit anti-PP2A B56 Epsilon	Aviva Systems Biology	Cat# RP56694_P050
rabbit anti-Hec1 pS44	DeLuca et al. ⁴²	N/A
rabbit anti DSN1 pS100	Welburn et al. ⁴³	N/A
rabbit anti-KNL1 pT943/pT1155	Cell Signaling Technology	Cat# #40758
mouse anti- α -Tubulin DM1 α	Sigma-Aldrich	Cat# T9026
mouse anti-Aurora A	Cell Signaling Technology	Cat# 1F8
Rabbit anti-Aurora A pT288	Cell Signaling Technology	Cat# C39D8
Rabbit anti-TACC3	Gergely et al. ⁴⁴	N/A
mouse anti-TPX2	Cell Signaling Technology	Cat# D9Y1V
rabbit anti-Aurora B pT232	Rockland	Cat# 600-401-677
rabbit anti-MCAK pS95	Abcam	Cat# AB74146
rabbit anti-Hec1 pT31	Kucharski et al. ²⁶	N/A
rabbit anti-BOD1L1	Higgs et al. ¹⁸	N/A
rabbit anti-BOD1L1	Genetex	Cat# #GTX119946
rabbit anti-GST	Molecular Probes	Cat# A-5800
Mouse TrueBlot® ULTRA: rat Anti-Mouse IgG	Rockland	Cat# 18-8817-33
Goat Polyclonal Antibody (Horseradish Peroxidase), Peroxidase AffiniPure Goat Anti-Rabbit IgG (H + L)	Jackson ImmunoResearch	Cat# 111-035-003
Goat Polyclonal Antibody (Horseradish Peroxidase), Peroxidase AffiniPure Goat Anti-Mouse IgG (H + L)	Jackson ImmunoResearch	Cat# 115-035-003
Bacterial and virus strains		
NEB Stable E. Coli	NEB	Cat# C3040H
BL21 E. coli	NEB	Cat# C2530H
Chemicals, peptides, and recombinant proteins		
Nocodazole	VWR	Cat# 80058-500
Okadaic acid	LC Labs	Cat# O-5857
MLN8237	Selleck	Cat# S1133
ZM447439	Tocris Bioscience	Cat# #2458/10
UMK57	Aobiouss	Cat# AOB8668
Lipofectamine™ 2000	ThermoFisher Scientific	Cat# 11668027
Clarity ECL	Bio-Rad	Cat# #1705060
Protein G agarose, Fast Flow	Millipore Sigma	Cat# 16-266
dimethyl pimelimidate	Sigma Aldrich	Cat# 80490-5G
β -Glycerophosphate disodium salt hydrate	Sigma Aldrich	Cat# G9422-10G
Thymidine	Sigma Aldrich	Cat# T1895-5G
Glutathione-Agarose	Sigma Aldrich	Cat# G4510

(Continued on next page)

Continued

REAGENT or RESOURCE	SOURCE	IDENTIFIER
ProQ Diamond phosphoprotein stain	ThermoFisher Scientific	Cat# P33301
Anti-FLAG affinity gel	Sigma Aldrich	Cat# A2220-5ML
Critical commercial assays		
TMT 6-plex	ThermoFisher Scientific	Cat# 90061
Deposited data		
UMK57 resistance screen: total protein	This study	PXD058821
UMK57 resistance screen: phosphoprotein	This study	PXD058823
BOD1L1 interactome	This study	PXD058824
Experimental models: Cell lines		
SW620	ATCC	CCL-227
HCT116	ATCC	CCL-247
HeLa	ATCC	CCL-2
U2OS	ATCC	HTB-96
HEC1	Tyler Curiel	N/A
293T	Jose Teodoro	N/A
RPE1	Arnold Hayer	N/A
Oligonucleotides		
shRNA #1 targeting BOD1L1 5'- GCCAATGATGCCATGTCGATA-3'	This paper	N/A
shRNA #1 targeting BOD1L1 5'- ACTCGCATGTATCCAAGTAAA-3'	This paper	N/A
Recombinant DNA		
pLKO.1 – TRC cloning vector	Moffat et al. ⁴⁵	Addgene Plasmid #10878
pLKO.1 shBOD1L1 #1	This study	N/A
pLKO.1 shBOD1L1 #2	This study	N/A
pVSV-G	Gee et al. ⁴⁶	Addgene Plasmid #138479
pCMV-dR8.2 dvpr	Stewart et al. ⁴⁷	Addgene Plasmid #8455
pET21-GFP-AURKA	Bertolin et al. ⁴⁸	Addgene Plasmid #99875
pGEX-5x-BOD1L F6 (aa 2399–3051 of BOD1L)	Bayley et al. ¹⁶	N/A
pGEX-5x-BOD1L F6 (aa 2399–3051 of BOD1L) S2631A, S2954A, T2956A, S2958A, S2973A, S975A (F6A)	This study	N/A
p3XFLAG-PPP2R5C myc CMV26	This study	N/A
pHAT 6XHis-KIF4A 799-1232-eGFP-Strep	This study	N/A
Software and algorithms		
Monocle	Rad et al. ⁴¹	N/A
SEQUEST	Yates ⁴⁹	N/A
Nikon Elements batch deconvolution software version 5.21.00	Nikon	N/A
Nikon NIS-Elements software version 4.30.02	Nikon	N/A
Fiji	Schindelin et al. ⁵⁰	N/A
Graphpad Prism version 8.4.3	GraphPad Software	N/A
R version 4.2.1.	R Core Team ⁵¹	N/A
R package <i>survival</i>	Therneau et al. ⁵²	N/A
R package <i>survminer</i>	Alboukadel et al. ⁵³	N/A
Other		
Chemi-doc MP	Bio-Rad	Cat# 12003154
Emulsiflex-C5	Avestin	N/A
Nikon Eclipse Ti	Nikon	N/A
Clara CCD camera	Andor Technology	N/A

EXPERIMENTAL MODEL AND STUDY PARTICIPANT DETAILS

SW620 (male), HCT116 (male), HeLa (female) and U2OS (female) cells were obtained from the ATCC. HEC1 (female) cells were a gift from Tyler Curiel. 293T (female) cells were a gift of Jose Teodoro. RPE1 (female) cells were a gift of Arnold Hayer. All cells were grown at 37°C in a humidified environment with 5% CO₂. SW620, HeLa, 293T and U2OS cell lines were grown in Dulbecco's modified Eagle medium (Corning #15-017-CM) containing 10% FCS (Hyclone #82013-586), 250 µg/L Amphotericin B (VWR #82026-728), 50 U/mL penicillin and 50 µg/mL streptomycin (ThermoFisher Scientific #15140122). HCT116 and HEC1 cells were grown in McCoy's 5A medium with the same supplements. RPE1 cells were grown in DMEM-F12 with the same supplements. Cells were verified to be free of mycoplasma by frequent staining of plated cells with DAPI. No contamination was observed.

METHOD DETAILS

Inhibitors and reagents

The CENP-E inhibitor GSK-923295 (MedChemExpress LLC # HY-10299) was used at 200 nM. NOC (VWR #80058-500) was used at 100–500 ng/mL. STLC (Tocris #2191) was used at 25 µM. ProTAME (Concept Life Sciences custom synthesis) was used at 25 µM. Okadaic acid (LC Labs O-5857) was used at 200 nM. RO-3306 (Selleck #S7747) was used at 10 µM. AZ3146 (R&D Systems #3994/10) was used at 2 µM. BI2536 (Synthesized in-house) was used at 100 nM. MLN8237 (Selleck #S1133) was used at 10–50 nM. ZM447439 (Tocris Bioscience #2458/10) was used at 2 µM. UMK57 (Aobious #AOB8668) was used at 100 nM.

Plasmids and cloning

The pLKO.1 – TRC cloning vector was a gift from David Root (Addgene plasmid # 10878; <http://n2t.net/addgene:10878>; RRID:Addgene_10878). The shRNA sequences were cloned into the AgeI and EcoRI sites of the plasmid using standard cloning techniques. The DNA constructs were then verified by Sanger sequencing and amplified by maxiprep (Qiagen #12162). Lentiviruses were produced by co-transfection of 293T/17 cells with pVS-G and pdVPR29.1 plasmids. 48 h later, the virus containing supernatant was harvested, briefly centrifuged to remove cell debris and frozen at –80°C until further use.

Proteomic screens

For the total protein and phospho-proteomic screen, ~80% confluent cells were re-plated at a 1:10 dilution on 15 cm plates. 3 dishes were treated with DMSO and 3 with UMK57. 72 h later, 2 dishes each of control and UMK57 treated cells were treated with 2.5 mM thymidine, and continuing DMSO/UMK57 treatment. 24 h following thymidine addition, it was washed out with 2 washes of 5 mL PBS, and then fresh media added containing 100 ng/mL nocodazole, still containing DMSO/UMK57. 16 h later the DMSO treated cells were treated for 1 h with UMK57. The mitotic cells were harvested by shakeoff, centrifugation followed by a wash with 5 mL PBS, re-centrifugation and finally frozen at –80°C before mass spectrometry analysis. Separately, following the 72 h DMSO/UMK57 treatment, the remaining dishes were trypsinized and re-plated on glass coverslips for microscopy analysis.

Sample preparation: Samples were prepared essentially as previously described,^{54,55} with a few modifications. Cells were lysed in 8M urea, 200 mM EPPS, pH 8.5, supplemented with 1X Pierce protease and phosphatase inhibitors. The resuspended samples were passed through a 1.5-inch 21-gauge needle to ensure DNA were sheared. Protein concentration was determined for each sample with BCA. Samples were reduced with 5 mM TCEP at room temperature for 20 min, alkylated with 10 mM iodoacetamide at room temperature for 20 min in the dark, and then quenched with 10 mM DTT at room temperature for 20 min in the dark. Methanol-chloroform precipitation was performed prior to protease digestion. In brief, 4-parts neat methanol were added to each sample and vortexed, 1-part chloroform was added to the sample and vortexed, and 3-parts water was added to the sample and vortexed. The sample was centrifuged at 14,000 RPM for 2 min at room temperature and subsequently washed once with 100% methanol. Samples were resuspended in 200 mM EPPS, pH 8.5 and digested at room temperature for 14 h with Lys-C protease at a 50:1 protein-to-protease ratio. Trypsin was then added at a 100:1 protein-to-protease ratio and the reaction was incubated for 6 h at 37°C.

Fe³⁺-NTA phosphopeptide enrichment: Following digestion with Lys-C and trypsin, peptides were desalting by using 100 mg SepPak columns. The elutions were dried via vacuum centrifugation and the phosphopeptides were enriched with the High-Select Fe3+-NTA Phosphopeptide Enrichment Kit according to manufacturer's specifications using approximately 4 mg protein digest per enrichment column. The elutions were dried via vacuum centrifugation, while the flow-throughs were saved for subsequent whole proteome analysis.

TMT labeling: In general, we estimate that at most 20 µg of phosphopeptides were enriched from 4 mg of total peptide. We added 40 µg of TMT 6-plex reagent (Thermo-Fisher) to the peptides along with acetonitrile to again achieve a final acetonitrile concentration of approximately 30% (v/v) in a total volume of 50 µL. Following incubation at room temperature for 1 h, the reaction was quenched with hydroxylamine to a final concentration of 0.3% (v/v). The sample was vacuum centrifuged to near dryness and subjected to C18 solid-phase extraction (SPE, Sep-Pak). Offline basic pH reversed-phase (BPRP) fractionation: We fractionated the peptide samples using BPRP HPLC. We used an Agilent 1200 pump equipped with a degasser and a UV detector. Peptides were subjected to a 50-min linear gradient from 5% to 35% acetonitrile in 10 mM ammonium bicarbonate pH 8 at a flow rate of 0.6 mL/min over an Agilent 300Extend C18 column (3.5 µm particles, 4.6 mm ID and 250 mm in length). The peptide mixture was fractionated into a total of 96 fractions, which were consolidated into 12 super-fractions. Samples were subsequently acidified with 1% formic acid and vacuum

centrifuged to near dryness. Each consolidated fraction was desalted by StageTip, and reconstituted in 5% acetonitrile, 5% formic acid for LC-MS/MS processing.

Liquid chromatography and tandem mass spectrometry: Mass spectrometric data were collected on an Orbitrap Lumos mass spectrometer coupled to a Proxeon NanoLC-1200 UHPLC (ThermoFisher Scientific). The 100 μ m capillary column was packed in-house with 35 cm of Accucore 150 resin (2.6 μ m, 150 \AA ; ThermoFisher Scientific). Data were acquired for 180 min per fraction. MS1 spectra were acquired at 120 K resolving power for a maximum of 50 ms in the Orbitrap, and features were filtered for mono-isotopic peak assignment and charge states 2–6. MS2 spectra were acquired by selecting the top 10 most abundant features. MS2 spectra were acquired via collisional induced dissociation (CID), in the ion trap with an automatic gain control (AGC) of 20K, quadrupole isolation width of 0.5 m/z and a maximum ion time of 120 ms with Multistage Activation turned on. For MS3 acquisition, a synchronous precursor selection (SPS) of 10 fragments ions was acquired for a maximum of 150 ms with an AGC of 300K and a normalized collision energy of 65.

Data analysis: Database searching included all entries from the mouse UniProt Database (downloaded: 2014). The database was concatenated with one composed of all protein sequences for that database in the reversed order.⁵⁶ Raw files were converted to mzXML, and monoisotopic peaks were re-assigned using Monocle.⁵⁷ Searches were performed with SEQUEST⁴⁹ using a 20-ppm precursor ion tolerance. TMT labels on lysine residues and peptide N-termini (+229.1629 Da), as well as carbamidomethylation of cysteine residues (+57.021 Da) were set as static modifications, while oxidation of methionine residues (+15.995 Da) and phosphorylation (+79.966) were set as variable modifications. Peptide-spectrum matches (PSMs) were adjusted to a 1% false discovery rate (FDR) using a linear discriminant after which proteins were assembled further to a final protein-level FDR of 1% analysis.⁵⁸ Ascore was used to determine site localization,⁵⁹ with a score of 13 denoting 95% confidence for a specified phosphorylation site. Phosphorylation sites were quantified by summing reporter ion counts across all matching PSMs. Peptides were filtered to include only those with a summed signal-to-noise (SN) \geq 100 across all TMT channels as well as an isolation specificity (“isolation purity”) of at least 0.5.

Whole proteome profiling

Sample preparation for whole proteome profiling: Flow-throughs from the phospho-enrichment described above, 50 μ g per replicate, were used for the whole proteome work for each sample.

TMT labeling: 120 μ g of TMTpro reagents (Thermo-Fisher; Lot # WL338745) were added to the peptides (50 μ g) along with acetonitrile to achieve a final acetonitrile concentration of approximately 30% (v/v) in a total volume of 100 μ L. Following incubation at room temperature for 1 h, the reaction was quenched with hydroxylamine to a final concentration of 0.3% (v/v). The sample was vacuum centrifuged to near dryness and subjected to C18 solid-phase extraction (SPE, Sep-Pak).

Offline basic pH reversed-phase (BPRP) fractionation: We fractionated the peptide samples using BPRP HPLC. We used an Agilent 1200 pump equipped with a degasser and a UV detector. Peptides were subjected to a 50-min linear gradient from 5% to 35% acetonitrile in 10 mM ammonium bicarbonate pH 8 at a flow rate of 0.6 mL/min over an Agilent 300Extend C18 column (3.5 μ m particles, 4.6 mm ID and 250 mm in length). The peptide mixture was fractionated into a total of 96 fractions, which were consolidated into 24 super-fractions (in a checkerboard-like pattern) of which 12 were used for data acquisition. Samples were subsequently acidified with 1% formic acid and vacuum centrifuged to near dryness. Each consolidated fraction was desalted by StageTip, and reconstituted in 5% acetonitrile, 5% formic acid for LC-MS/MS processing.

Liquid chromatography and tandem mass spectrometry: Mass spectrometric data were collected on an Orbitrap Fusion mass spectrometer coupled to a Proxeon NanoLC-1200 UHPLC (ThermoFisher Scientific). A 100 μ m capillary column was packed in-house with 35 cm of Accucore 150 resin (2.6 μ m, 150 \AA ; ThermoFisher Scientific). Data were acquired for 180 min per fraction. MS1 spectra were acquired at 120 K resolving power for a maximum of 100 ms in the Orbitrap, and features were filtered for mono-isotopic peak assignment and charge state of 2. MS2 spectra were acquired by selecting the top 10 most abundant features. MS2 spectra were acquired via collisional induced dissociation (CID), in the ion trap with an automatic gain control (AGC) of 9K, quadrupole isolation width of 0.7 m/z at Rapid Scan Rate. For MS3 acquisition, a synchronous precursor selection (SPS) of 10 fragments ions was acquired for a maximum of 200 ms with an AGC of 200K and a normalized collision energy of 55.

Data analysis. Searches were performed as described above but without phosphorylation variable modifications. Proteins were quantified by summing reporter ion counts across all matching PSMs. More specifically, reporter ion intensities were adjusted to correct for the isotopic impurities of the different TMTpro reagents according to manufacturer specifications. Peptides were filtered to include only those with a summed signal-to-noise (SN) \geq 100 across all TMT channels and isolation specificity of at least 0.5. The signal-to-noise (S/N) measurements of peptides assigned to each protein were summed (for a given protein) and each protein abundance measurement was scaled, such that the summed signal-to-noise for that protein across all channels equals 100, thereby generating a relative abundance (RA) measurement.

Transfections

200,000 SW620 cells were plated on glass coverslips in 12-well plates. 24 h following plating, they were transfected with 1 μ g plasmid DNA and 2.5 μ L Lipofectamine 2000 (ThermoFisher #11668027) in a total of 1 mL Opti-MEM media (ThermoFisher #31985070). Four hours following transfection, the media was changed for DMEM containing 2 μ g/ml puromycin. The cells were then assayed 48–72 h following addition of puromycin.

SDS-PAGE and western blot

Gels and blots were performed as described previously.⁶⁰ Prior to loading samples on gel, 4X Laemmli buffer (200 mM Tris pH 6.8, 4% SDS, 40% glycerol, 4% 2-mercaptoethanol, 0.12 mg/mL bromophenol blue) was added to a final dilution of 1X, and the samples were boiled for 5 min. Proteins were separated on SDS-PAGE gel using stacking gel (4% 29:1 acrylamide: Bis-acrylamide, 125mM Tris pH 6.8, 0.1% SDS, 0.1% ammonium persulfate, 0.1% TEMED) and (8–15% 29:1 acrylamide: Bis-acrylamide, 400 mM Tris pH 8.8, 0.1% SDS, 0.1% ammonium persulfate, 0.1% TEMED) at 120V until the bromophenol blue has run off or longer, as needed. Transfer onto nitrocellulose membrane was performed for at least 24 h at 30V under wet conditions in 1X transfer buffer (14.4 g/L glycine, 3.0 g/L Tris, 20% methanol). Conditions for western blots includes the use of 5% nonfat dry milk in TBS-T 0.5% (50 mM Tris [pH 7.2], 150 mM NaCl, 0.5% Tween 20) for blocking and TBS-T 0.5% for washing. 4 washes for 10 min each were performed after primary and secondary antibody incubation periods. The bands were visualized by enhanced chemiluminescence using Clarity (Bio-Rad #1705060) using a Bio-Rad ChemiDoc MP.

Immunoprecipitation

Protein-G beads were first crosslinked to the antibody by incubating the beads and antibody overnight on a rotating platform. The beads were then washed with PBS and then crosslinking solution (20mM dimethyl pimelimidate, 0.3M HEPES in ice-cold water). The beads were then incubated in crosslink solution for 10 min at room temperature. The solution is then discarded, and the incubation repeated in fresh crosslink buffer, which is performed three times. The beads are then washed in PBS twice and twice with lysis buffer prior to use.

SW620 cells from confluent 15 cm dishes were split 1:5. 48 h later, 2.5 mM thymidine was added. 24 h following thymidine addition, it was washed out with 2 5mL washes with PBS. Fresh media containing 100 ng/mL nocodazole was then added. 16 h later, the cells were harvested by scraping, washed once with cold PBS, and lysed in the following buffer: 0.5% NP40, 100 mM NaCl, 50 mM tris pH 7.4, 10 mM glycerol 2-phosphate. Cells were lysed on ice for 20 min before centrifuging at 15,000 x g for 20 min at 4°C. The supernatant was transferred to a fresh tube, and input sample set aside. 10 µL of packed volume protein G beads cross-linked to antibody were added to each sample for 2 h on a rotating platform at 4°C. The beads were then washed 5 times in lysis buffer and dried using a 30 g needle attached to a vacuum line. 30–100 µL of 1X sample buffer were added to the beads before elution by boiling and loading on gel.

Identification of BOD1L1 interacting proteins

Excised gel bands were cut into approximately 1 mm³ pieces. Gel pieces were then subjected to a modified in-gel trypsin digestion procedure.⁶¹ Gel pieces were washed and dehydrated with acetonitrile for 10 min followed by removal of acetonitrile. Pieces were then completely dried in a speed-vac. Rehydration of the gel pieces was with 50 mM ammonium bicarbonate solution containing 12.5 ng/µL modified sequencing-grade trypsin (Promega, Madison, WI) at 4°C. After 45 min, the excess trypsin solution was removed and replaced with 50 mM ammonium bicarbonate solution to just cover the gel pieces. Samples were then placed in a 37°C room overnight. Peptides were later extracted by removing the ammonium bicarbonate solution, followed by one wash with a solution containing 50% acetonitrile and 1% formic acid. The extracts were then dried in a speed-vac (~1 h). The samples were then stored at 4°C until analysis. On the day of analysis the samples were reconstituted in 5–10 µL of HPLC solvent A (2.5% acetonitrile, 0.1% formic acid). A nano-scale reverse-phase HPLC capillary column was created by packing 2.6 µm C18 spherical silica beads into a fused silica capillary (100 µm inner diameter x ~30 cm length) with a flame-drawn tip.⁶² After equilibrating the column each sample was loaded via a Famos auto sampler (LC Packings, San Francisco CA) onto the column. A gradient was formed and peptides were eluted with increasing concentrations of solvent B (97.5% acetonitrile, 0.1% formic acid). As peptides eluted they were subjected to electrospray ionization and then entered into an LTQ Orbitrap Velos Pro ion-trap mass spectrometer (Thermo Fisher Scientific, Waltham, MA). Peptides were detected, isolated, and fragmented to produce a tandem mass spectrum of specific fragment ions for each peptide. Peptide sequences (and hence protein identity) were determined by matching protein databases with the acquired fragmentation pattern by the software program, Sequest (Thermo Fisher Scientific, Waltham, MA).⁴⁹ All databases include a reversed version of all the sequences and the data was filtered to between a one and 2% peptide false discovery rate.

RNA interference

Gene knockdown was performed by cloning the following shRNA sequences into the PLKO1 vector and then transfecting cancer cells with 1 µg of plasmid DNA and 2.5 µL lipofectamine 2000 per mL according to the manufacturer's directions. Media was changed after 5 h, and puromycin added after 24 h.

BOD1L1-1: 5'- GCCAATGATGCCATGTCGATA-3'
BOD1L1-2: 5'- ACTCGCATGTATCCAAGTAAA-3'

Gene knockdown in RPE1 cells was performed by transducing them with lentivirus produced in 293T/17 cells transfected with 4.5 µg pLKO plasmids together with 1.5 µg pVS-G and 3.3 µg pdVPR29.1 with 22.5 µL lipofectamine 2000 in 6 mL Opti-MEM media. After 24 h, the media was changed for 8 mL DMEM. Virus was harvested at 48 and 72 h post-transfection. The amount of virus used on target cells was such to induce approximately 5% cell death following puromycin selection.

Immunofluorescence

Following treatments, cells were pre-extracted in PHEM buffer (60 mM PIPES, 25 mM HEPES, pH 6.9, 10 mM EGTA, and 4 mM MgSO₄, 1% Triton X-100, 10 mM glycerol 2-phosphate) for 10 min at 4°C and then fixed in 4% paraformaldehyde in PBS at room temperature for 20 min. The remaining steps were performed at room temperature. The cells were then washed twice with PBS before blocking with ADB (10% serum, 0.1% Triton X-100 in PBS) for 15 min. Primary antibodies were then diluted in ADB and used at the indicated dilution. Secondary antibodies were diluted in ADB. After incubation with antibodies, the cells were washed three times with PBS 0.1% Triton X-100. Finally, the cells were counterstained with DAPI and mounted on slides using ProLong Gold antifade reagent (ThermoFisher Scientific #P36934).

***In vitro* analysis of BOD1L1**

BOD1L1 fragments were produced in the E. Coli strain BL21 expressing GST-BOD1L1 fragments.¹⁶ The bacteria were suspended in 50 mM Tris pH7.5, 250 mM NaCl, 10% glycerol, 0.1% 2-mercaptoethanol and processed in an emulsiflex high-pressure homogenizer (Avestin). The lysate was then ultracentrifuged at 45Ti rotor at 25000 RPM for 45 min. 200 µL of packed glutathione agarose was then added for 2 h on a rotating platform. The agarose was then washed 5 times in buffer. Purified proteins were then eluted 3 times using 200 µL buffer plus 25 mM reduced glutathione, which were combined and then dialyzed against 0.4X TBS. Glycerol was then added to 10% and the proteins frozen until further use. GFP-AuroraA-6XHis⁴⁸ was also produced in the E. Coli strain BL21. The bacteria was suspended in 25 mL buffer A (50 mM NaPO₄, 10 mM Imidazole, 300 mM NaCl, 10% Glycerol, pH 8) and processed as for the GST-BOD1L1. 1 mL Ni-NTA agarose was then added to the lysate for 2 h on a rotating platform. The agarose was then washed, and purified proteins eluted with buffer A containing 300mM imidazole and then dialyzed against 0.4X TBS. Glycerol was then added to 10% and the proteins frozen until further use. Kinase reactions were performed by mixing GST-BOD1L1, GFP-Aurora A-6XHis, 100 µM ATP in kinase buffer 50 mM Tris pH 7.2, 25 mM NaCl, 10mM MgCl₂ 1mM DTT, 0.01% Triton X-100 for 1 h at 37°C. The reactions were stopped by addition of 4X SDS sample buffer, and half the reaction loaded on SDS-PAGE gel. The gels were then stained with ProQ Diamond phosphoprotein stain (Thermo Scientific) according to the manufacturer's instructions and subsequently with Coomassie blue. We performed GST-pulldowns essentially as described previously.¹⁶ Briefly, SW620 mitotic nuclear extracts were incubated with 1 µg of GST-fusion protein or purified GST as a control on a rotating platform for 3 h. Bound proteins were then purified via binding to glutathione Sepharose (GE Healthcare) and washed. Samples were then analyzed by Western blot. Mutations in BOD1L1 (S2631A, S2954A, T2956A, S2958A, S2973A, S975A: F6A) and (S2631D, S2954D, T2956E, S2958D, S2973D, S975D: F6D) were created by custom DNA synthesis of the mutated fragments (Twist Bio) and cloning them into the same SalI/NotI restriction enzyme sites as the Wt F6 fragments.

***In vitro* phosphatase reaction**

3X10⁶ 293T cells were plated on 15 cm dishes (1 plate for 2 reactions) and transfected with 20 µg 3XFLAG-PPP2R5C or empty vector via calcium phosphate. 48 h following transfection, the cells were harvested and lysed in tris-buffered saline with 0.5% NP40 (2 mL/plate). 3XFLAG-PPP2R5C was then purified by immunoprecipitation using 10 µL of packed anti-FLAG affinity gel per reaction (#A2220-5ML; Sigma-Aldrich). The affinity gel was then washed 3 times in lysis buffer and once in wash buffer (50 mM Tris, 50 mM NaCl, 0.1% NP40) and the buffer removed leaving the beads just damp. GST control or BOD1L1 F6 purified as above were then added along with GFP-KIF4A 799–1232 phosphorylated *in vitro* by GFP-His-Aurora A plus 1 mM MnCl₂ and 100 nM MLN8237 in a total volume of 50 µL. The samples were then incubated at 37°C with mixing at 700 rpm until the reaction was stopped by addition of 4X sample buffer at indicated time points. One-quarter of the reaction was then run on SDS-PAGE gel, which was then stained with ProQ-Diamond, imaged and then subsequently with Coomassie and re-imaged.

Microscopy

Images were acquired with a Nikon Eclipse Ti microscope equipped with a cooled charge-coupled device Clara camera (Andor Technology) controlled by Nikon NIS-Elements software version 4.30.02. Images were acquired in 0.15–0.4 µm sections using a plan apo 1.4 numerical aperture 100X (kinetochore analysis) or 60× (lagging chromosome analysis) oil-immersion objective using 1X1 binning. Samples were illuminated using an X-cite light source (Excelitas Technologies Corp). All image analysis, adjustment and cropping was performed using Fiji software.⁵⁰ Image deconvolution was performed using Nikon Elements batch deconvolution software version 5.21.00 on automatic mode. All kinetochore intensity analysis was performed on the raw images, except for microtubule intensity determination for which deconvolution was performed prior to analysis. Line scans were performed on the deconvoluted images in Fiji and the data was then exported to Graphpad Prism. All images of BOD1L1 selected from SW620 cells are deconvolved, maximum intensity projections of 3 optical slices closest to the center of the cell. Images of other stained proteins are deconvolved maximum intensity projections of the full image stack. Where shown, insets are from single optical Z-slices. Images were selected to represent the mean quantified data. Quantification of kinetochore staining intensity was performed by first determining the brightest plane for which a given kinetochore appears. Then, an outline was drawn using the ellipse tool. The integrated intensity was determined by multiplying the average intensity by the area of the kinetochore. Background levels of staining were determined by saturating the brightness and contrast settings to find the darkest spot within the chromatin containing area and were subtracted from the intensity of the kinetochore. AurKA pT288 was quantified by first creating a sum projection of the image. Then, an outline was drawn around the whole cell, and the fluorescence intensity measured. The background-subtracted, normalized integrated intensities for all

cells were then plotted. To quantify levels of cold-stable microtubules, images were first deconvolved. Then, A sum-intensity projection was created in Fiji. Viewing the ACA channel, a rectangle was drawn that was 2 μm wide in the pole-pole axis, and as long as the furthest centromeres in the metaphase plate. Then, switching to the tubulin channel, the average tubulin intensity was measured in the rectangle. From the average intensity value, the minimum intensity value was used as the background level and subtracted. The Background-subtracted intensity values were then averaged across all of the cells that were analyzed for each condition and experimental repeat.

For live-cell microscopy, cells were transfected with 0.5 μg of mCherry-H2B-expressing plasmid together with pLKO vectors. After selection with puromycin, the cells were washed twice with PBS, given fresh medium and moved to a Tokai Hit incubation chamber with CO_2 and temperature control on the microscope. The cells were imaged every 5 min at 20 \times magnification for 48 h with 2X2 binning.

Antibodies

The following antibodies were used for immunofluorescence (IF) and/or immunoblotting (IB): human anti-ACA (Geisel School of Medicine; IF at 1:2000), mouse anti-Hec1 (Santa Cruz C-11; IF, IB at 1:1000), mouse anti-PP2AR1A (Santa Cruz SC-74580; IB at 1:500), mouse anti-PP2AC (Santa Cruz SC-166034; IB at 1:500), rabbit anti-PP2A B56 Alpha ([MyBioSource.com](#) MBS8524809; IB at 1:500), mouse anti-PP2A B56 Beta (Santa Cruz E-6; IB at 1:500), mouse anti-PP2A B56 Gamma (Santa Cruz A-11; IB at 1:500), mouse anti-PP2A B56 Delta (Santa Cruz H-11; IB at 1:500), rabbit anti-PP2A B56 Epsilon (Aviva Systems Biology RP56694_P050; IB at 1:500), rabbit anti-Hec1 pS44 (gift of Jennifer DeLuca; IF at 1:500),⁴² rabbit anti-DSN1 pS100 (gift of Iain Cheeseman; IF at 1:250),⁴³ rabbit anti-KNL1 pT943/pT1155 (Cell Signaling #40758), mouse anti- α -Tubulin DM1 α (Sigma-Aldrich; IF at 1:4000-1:10,000), mouse anti-Aurora A (Cell Signaling Technology 1F8; IF at 1:1000), Rabbit anti-Aurora A pT288 (Cell Signaling Technology C39D8; IF at 1:500), Rabbit anti-TACC3 (gift of Jordan Raff; IF at 1:1000),⁴⁴ mouse anti-TPX2 (Cell Signaling Technology D9Y1V; IF at 1:1000), rabbit anti-Aurora B pT232 (Rockland 600-401-677; IF/IB at 1:1000), rabbit anti-MCAK pS95 (Abcam #AB74146; IF/IB at 1:500), rabbit anti-Hec1 pT31²⁶ (IF at 1:100,000, WB at 1:1000), rabbit anti-BOD1L1 (IF at 1:1000) (gift of Grant Stewart¹⁸), rabbit anti-BOD1L1 (Genetex #GTX119946; WB at 1:500), rabbit anti-GST (Molecular Probes #A-5800; WB at 1:1000). Secondary antibodies used were highly cross-adsorbed Alexa Fluor 488, 594 and 647 raised in donkey or goat (Invitrogen; IF at 1:1000), horseradish peroxidase (Bio-Rad; IB at 1:10000-10,0000), Mouse TrueBlot ULTRA: rat Anti-Mouse IgG (Rockland 18-8817-33; IB at 1:1000), Anti-IgG (H + L) Goat Polyclonal Antibody (Horseradish Peroxidase), Peroxidase AffiniPure Goat Anti-Rabbit IgG (H + L) (IB at 1:5000), Goat Polyclonal Antibody (Horseradish Peroxidase), Peroxidase AffiniPure Goat Anti-Mouse IgG (H + L) (IB at 1:5000).

QUANTIFICATION AND STATISTICAL ANALYSIS

Statistical analysis of cell biology data

All statistical tests were performed using Graphpad Prism version 8.4.2. Except where indicated, all experiments were performed as 2-3 independent biological repeats. In most IF experiments, 20 cells per repeat were analyzed, and 25 kinetochores for each cell measured. Experiments with other numbers are noted in the figure legends. For anaphase error rates, 100 anaphases per condition were assessed for each of 3 independent biological experiments. Statistical significance was calculated between indicated conditions using two-tailed *t*-tests or Dunnett's multiple comparison test. For these tests, the data distribution was assumed to be normal but this was not formally tested.

Population data, and statistical analysis

The cBioPortal for Cancer Genomics was used to query and visualize *BOD1L1* alterations in data from The Cancer Genome Atlas (TCGA). Then, TCGA PanCancer Atlas cancer specific clinical and *BOD1L1* alteration data was downloaded via cBioPortal for Cancer Genomics for cancer types where *BOD1L1* alteration was most frequent: uterine corpus endometrial carcinoma TCGA-UCEC PCA ($n = 529$), lung adenocarcinoma TCGA-LUAD ($n = 667$), cutaneous melanoma TCGA-SKCM ($n = 448$), stomach adenocarcinoma TCGA-STAD ($n = 440$), and lung squamous cell carcinoma TCGA-LUSC ($n = 487$). All statistical analysis was conducted in R version 4.2.1. Survival analysis using Kaplan-Meier plots and Cox Proportional-Hazards models was conducted using R package *survival* and plotted using R package *survminer*. Univariate Kaplan-Meier survival strata were plotted for altered *BOD1L1* status in each cancer type to assess five-year overall survival status. Cox Proportional Hazards models for each cancer type tested association of *BOD1L1* alteration status with adjustment for patient age, sex (excepting uterine), and tumor stage or grade. Using Fisher's exact tests and patient data from all TCGA-PanCancer Atlas cancer datasets ($n = 10,967$ from 32 cancer types), we tested whether *BOD1L1* alterations were exclusive of alterations to other Aurora A-BOD1L1- PP2A gene pathway members.